

52p

N 63 16294

code-1



TECHNICAL NOTE

D-1790

HEAT-TRANSFER AND PRESSURE DISTRIBUTIONS AT MACH NUMBERS
OF 6.0 AND 9.6 OVER TWO REENTRY CONFIGURATIONS FOR
THE FIVE-STAGE SCOUT VEHICLE

By Paul F. Holloway and James C. Dunavant

Langley Research Center
Langley Station, Hampton, Va.

NATIONAL AERONAUTICS AND SPACE ADMINISTRATION
WASHINGTON

May 1963

NATIONAL AERONAUTICS AND SPACE ADMINISTRATION

TECHNICAL NOTE D-1790

HEAT-TRANSFER AND PRESSURE DISTRIBUTIONS AT MACH NUMBERS
OF 6.0 AND 9.6 OVER TWO REENTRY CONFIGURATIONS FOR
THE FIVE-STAGE SCOUT VEHICLE

By Paul F. Holloway and James C. Dunavant

SUMMARY

Heat-transfer and pressure distributions have been obtained for a five-stage Scout reentry configuration (both with and without a calorimeter nose cap) over an angle-of-attack range of 0° to 30° in the Langley 20-inch Mach 6 tunnel and 0° to 25° in the Mach number 9.6 nozzle of the Langley 11-inch hypersonic tunnel. The results indicate that modified Newtonian theory gives a good prediction of the trends of the pressure-distribution data. At an angle of attack of 0° , Lees' theory is shown to predict reasonably well the heat-transfer distribution over the blunt nose. Variation of Reynolds number and Mach number has virtually no effect on the heat-transfer distributions through the angle-of-attack range. The velocity-gradient correlation of Boisson and Curtiss is shown to give a good prediction of the stagnation heating level at an angle of attack of 0° .

INTRODUCTION

As a part of the National Aeronautics and Space Administration's space research program, an investigation of the aerothermodynamic effects of reentry into the earth's atmosphere at hypervelocity speeds is currently being conducted with a five-stage Scout vehicle. During a flight test, the first two stages of the Scout configuration boost the vehicle out of the atmosphere on the ascent phase of the flight, and the three remaining stages accelerate the vehicle on the descent phase of the flight to a maximum reentry velocity of approximately 30,000 feet per second. A detailed description of an early version of the Scout vehicle is given in reference 1.

In support of this project, the pressure and heat-transfer distributions of an early version of the reentry nose cone, both with and without the calorimeter nose cap, have been obtained at Mach numbers of 6.0 and 9.6. The objectives of these wind-tunnel experiments were to determine the maximum heat-transfer rate and the heat-transfer distributions at various angles of attack to implement the design of the spacecraft heat protection and also to provide a comparison for the flight heating results.

The purpose of this report is to present the heat-transfer and pressure distributions over a fifth-stage Scout reentry spacecraft, both with and without the calorimeter nose cap. The angle-of-attack range was 0° to 30° at a Mach number of 6.0 and 0° to 25° at a Mach number of 9.6. The Reynolds number of the heat-transfer tests at 0° angle of attack has been varied over a wide range so that the effect of this parameter on the laminar heat transfer at hypersonic speeds may be ascertained. Also, by comparison of the heat-transfer data for Mach numbers of 6.0 and 9.6, the combined effect of Reynolds number and Mach number on laminar heat transfer at angle of attack is observed. Finally, the effect of model size and test techniques on the accuracy of heat-transfer tests is discussed.

SYMBOLS

c_w	specific heat of model construction material
C_p	pressure coefficient, $\frac{p_l - p_\infty}{q_\infty}$
D	diameter of curvature of spherical segment nose, $2r_{\text{hemi}}$
$\frac{dT_w}{dr}$	time derivative of measured wall temperature
h	heat-transfer coefficient, defined in equation (1)
K	thermal conductivity of air
M	Mach number
N_{Pr}	Prandtl number
p	pressure
q	dynamic pressure
r	nose reference length (distance from cone center line to intersection of corner radius and cone, see fig. 1)
r_{hemi}	radius of curvature of spherical segment nose
r_l	radius of cross section at a longitudinal station
R_r	free-stream Reynolds number based on r
s	surface distance measured from 0° angle-of-attack stagnation point

t	local skin thickness
T	temperature
u	velocity
x	distance along longitudinal axis measured from stagnation point at 0° angle of attack
α	angle of attack referenced to axis of cone
β	velocity gradient, du/ds
δ	cone half-angle
η	angle between free-stream velocity vector and a vector normal to body surface
μ	viscosity
ρ	density
τ	time
ϕ	meridian angle defined in figure 1

Subscripts:

aw	adiabatic wall conditions
l	local conditions
s	stagnation point
t	total
w	wall
∞	free-stream conditions
σ	free-stream conditions immediately behind normal shock

CONFIGURATION CONCEPTS

In some instances, shapes of reentry bodies may be dictated by requirements other than aerodynamic. Such was the case in the design of the two reentry nose cones investigated in this report. The design of the fifth stage of a Scout vehicle designated to reenter the earth's atmosphere at speeds greater than orbital velocity was dictated by the mission requirements and the dimensional

limitations set by the booster stages. The maximum length and diameter of the reentry stage were limited by booster and heat-shield considerations, and the minimum diameter was necessarily greater than that of the 17-inch spherical rocket motor of the fifth (payload) stage. Nose bluntness was dictated by the mission requirement that the reentry vehicle have a low maximum heating rate. Thus, the reentry shape evolved, a shape that was essentially a short, very blunt, low-angle cone. A slight modification to this shape was produced when a thin-shell, metal calorimeter was placed over the forward half of the flight reentry capsule, and the cone angle over that portion of the nose cone was thereby reduced. More details of the experiment are given in reference 2.

The final configurations of the flight reentry spacecraft differ from the configurations of this investigation in that the cylindrical afterbody was eliminated from the flight configuration, and the forward portion of the configuration after the calorimeter nose cap was jettisoned had a short cylindrical section aft of the nose-corner radius. Some longitudinal aerodynamic characteristics of several versions of the reentry configurations with and without the calorimeter nose cap are presented in references 2 and 3.

APPARATUS AND METHODS

Models

Sketches of the exterior shape of the models are shown in figure 1. Figure 1(a) shows configuration I, the shape without the calorimeter nose cap and figure 1(b), configuration II, the shape with the calorimeter nose cap. A total of eight models, two pressure models and two heat-transfer models of each of the two configurations were made (the larger of each twice the size of the smaller). The designations (a) and (b) will be used to refer to the large and small models, respectively. The smaller models were designed for test in the smaller $M = 9.6$ tunnel and the larger models, for the $M = 6.0$ tunnel. The pressure models were machined from solid stock and the relatively thick (about $1/8$ inch) walls were instrumented with 0.040 I.D. pressure orifices at locations given in table I. The heat-transfer models were made from Inconel sheet, spun in two pieces, and welded together at a point behind the corner radius. Thermocouples were not installed near the weld joint. The thickness of the models was 0.050 inch on the blunt nose and tapered to a 0.030-inch thickness on the conical portion, the taper beginning on the corner radius. (Local measured skin thicknesses are listed in table I.) Thermocouples were silver-soldered in holes drilled in the skin at locations also given in table I. Instrumentation was located in the windward half of the model (for positive angles of attack). Leeward data were obtained by testing the model at negative angles of attack.

Wind Tunnels

The tests were conducted at $M = 6$ in the Langley 20-inch hypersonic tunnel and in the $M = 9.6$ nozzle of the Langley 11-inch hypersonic tunnel. The 20-inch hypersonic tunnel is of the intermittent type operating from a stored air

supply at stagnation pressures from 19 to 38 atmospheres and a maximum stagnation temperature of 600° F. The tunnel exhausts to the atmosphere through a diffuser augmented by an air ejector. A more detailed description of the tunnel is given in reference 4. Most of the tests were made at a stagnation pressure of 24 atmospheres and temperatures of 500° F to 600° F, for which the corresponding Reynolds number per inch is approximately 0.48×10^6 ; however, for an angle of attack of 0°, both the small and large models were tested over a range of pressure and temperature to obtain unit Reynolds number (per inch) of 0.33×10^6 to 0.70×10^6 .

The $M = 9.6$ nozzle of the 11-inch hypersonic tunnel is a three-dimensional rectangular, contoured nozzle having a calibrated Mach number of 9.6 at the nominal test conditions of 46 atmospheres total pressure and 1200° F total temperature. The Reynolds number per inch for these test conditions is 0.10×10^6 . Only the small models were tested in this facility. The tunnel is also of an intermittent blowdown type but exhausts to a vacuum sphere and has a running time of 1 to 2 minutes. A more detailed description of the nozzle and some calibration data can be found in reference 5.

Methods

Pressures.— The model static pressures in the $M = 6$ tests were recorded by photographing a multiple-tube mercury manometer board. Tunnel stagnation pressure was measured on a calibrated Bourdon gage. This method leads to inaccuracies of any measured pressure of less than ± 2 percent.

For the $M = 9.6$ tests, the pressures were recorded on six-cell aneroid, recording type pressure instruments. Pressures were read 60 seconds after the flow was initiated to insure that the pressure in the cell was fully stabilized. Inaccuracy for any measured pressure in the $M = 9.6$ tests is less than $\pm 2\frac{1}{2}$ percent.

Heat transfer.— Aerodynamic heating was measured by the transient calorimetry technique by which the rate of heat storage in the model skin is measured. The models initially at room temperature were suddenly exposed to the airstream and the rate of temperature rise of the skin was measured as soon as possible while the model was in a nearly isothermal condition; hence conduction between the surface elements was a minimum. In the $M = 6$ facility, exposure of the model was accomplished by quickly injecting the model into the stream from a sheltered position beyond the tunnel wall. With injection, there was a cavity in the tunnel wall which led to interference effects on some of the leeward data. These effects are discussed subsequently. There was no cavity in the tunnel wall during the pressure tests. Injection was accomplished in less than 0.25 second.

In the $M = 9.6$ tests, the model was installed in the test section prior to start of the airflow. The heating rates were measured as soon as flow conditions (settling chamber pressure and temperature) stabilized and while the model was still at nearly isothermal conditions. Approximately 2 seconds were required to achieve these conditions.

DATA REDUCTION

The Mach number used in the reduction of the pressure and heat-transfer data for both the $M = 6$ and $M = 9.6$ tests was based on previous tunnel calibrations.

At $M = 6$, the thermocouple outputs were recorded on a Beckman 210 high-speed digital data recording system. The output voltage of each thermocouple was sampled at a rate of 40 times per second, converted to a binary digital system, and recorded on magnetic tape. The temperature-time data were fitted to a second-degree curve by the method of least squares, and the time derivative of temperature was computed on a card programmed computer.

At $M = 9.6$, the thermocouple outputs were continuously recorded on four 18-channel D'Arsonval type galvanometers. The time derivative of temperature was then determined graphically from the temperature-time curve.

The measured local heat-transfer coefficient was calculated from the following relation:

$$h = \frac{\rho_w c_w t \frac{dT_w}{dt}}{T_{aw} - T_w} \quad (1)$$

where T_w = Measured wall temperature and T_{aw} is given by

$$T_{aw} = T + \sqrt{N_{Pr}}(T_s - T) \quad (2)$$

where N_{Pr} was assumed to be 0.69 and the temperature T was calculated from an isentropic expansion of the flow from the stagnation-point pressure and temperature behind a normal shock wave to the measured local static wall pressure. The heat-transfer coefficients were not corrected for any lateral conduction of heat in the model skin at either $M = 6.0$ or $M = 9.6$.

For the $M = 6.0$ data, the heat-transfer coefficients were computed for a time interval of approximately 0.1 to 0.6 second after the model was injected into the airflow. The coefficients presented herein were calculated from a time derivative of temperature and a measured wall temperature determined at approximately 0.10 second after the model is in position in the tunnel. The maximum surface temperature increase was 25°F at the time at which the coefficients were calculated. The low skin-temperature increase together with the thin skin thickness minimized the conduction error. The exact skin thickness was measured at each thermocouple location. The repeatability of $M = 6.0$ heat-transfer data is generally within ± 5 percent. The maximum inaccuracy of the data in most regions is believed to be ± 10 percent. However, in the corner regions where the conduction is large, the data may be in error by as much as ± 20 percent.

For the $M = 9.6$ tests, by using a quick-starting technique and allowing the flow to stabilize before calculating the heat-transfer coefficients, the maximum surface temperature increase was 160°F . This relatively large increase compared with that of the $M = 6$ tests led to a higher conduction error, particularly in the corner region. The repeatability of the $M = 9.6$ heat-transfer data is generally within ± 10 percent. The inaccuracies of the data on many regions are also believed to be within ± 10 percent. However, in regions where the conduction is large, it will be shown later that the data may be in error by 50 percent or more.

RESULTS AND DISCUSSION

Schlieren Photographs

Figure 2 presents schlieren photographs of the two configurations at various angles of attack in both the Mach 6.0 20-inch hypersonic tunnel and the Mach 9.6 nozzle of the 11-inch hypersonic tunnel. These photographs were obtained during the pressure tests.

An effect of the different corner radii of the two configurations on the local flow in the corner region is evident in the comparison of figure 2(a) with figure 2(b) for the $M = 6$ tests. On configuration I(a) (fig. 2(a)), there is a small separation region apparent for $\alpha \leq 10^{\circ}$ as evidenced by the presence of a reattachment shock. The strength of the reattachment shock decreases as α is increased from 0° to 10° . Separation above an angle of attack of 10° is not apparent on the windward side of the model; however, in figure 2(b) the small separated region at the corner of configuration II(a), which has a much smaller corner radius, remains through the angle-of-attack range. Moreover, the separated region on configuration II(a) is much larger than that of configuration I(a) since reattachment occurs farther back along the cone surface. This separation is not observed in the schlieren photographs at $M = 9.6$ (fig. 2(c)).

No boundary-layer transition is evident from an examination of the schlieren photographs.

Pressure Distribution

In figures 3 and 4, the pressure distributions over configuration I, the reentry cone without the calorimeter nose cap, are presented for an angle-of-attack range of 0° to 30° at a Mach number of 6.0 (fig. 3) and 0° to 25° at a Mach number of 9.6 (fig. 4). Figures 5 and 6 present the pressure distributions over configuration II, the reentry cone with the calorimeter nose cap, for an angle-of-attack range of 0° to 30° at a Mach number of 6.0 (fig. 5) and 0° to 25° at a Mach number of 9.6 (fig. 6). In each figure, the experimental pressure distribution is compared with the distribution predicted by modified Newtonian theory for which

$$C_p = C_{p,s} \cos^2 \eta \quad (3)$$

where $C_{p,s}$ is the maximum (stagnation) pressure coefficient behind a normal shock wave at the calibrated free-stream Mach number.

General agreement of theory and experiment.- Comparison of the experimental pressure distributions with modified Newtonian theory in figures 3 to 6 shows good agreement of the trends of the data and in most cases of the local pressure. However, it should be pointed out that the deviation of theory and experiment in the corner region will lead to large differences in the experimental and theoretical velocity gradients for this region.

Spherical nose.- In figures 3 to 6 it can be seen that the pressures in the stagnation region are very well predicted for each configuration over the angle-of-attack range. However, as the subsonic flow over the spherical nose accelerates from the stagnation point toward the corner, there is an experimental pressure deviation below the Newtonian predictions for both configurations that increases as the distance from the stagnation point is increased for $\alpha \leq 15^\circ$. For $\alpha > 15^\circ$, the location of the maximum pressure does not move as far windward as Newtonian theory predicts so that the measured pressures over the spherical nose are higher than the theoretical pressures.

Corner region.- The surface pressure data on the corner radius of the configurations tested are always lower than modified Newtonian theory. (See figs. 3 to 6.) In figure 5, the effects of the separation region and reattachment shock on configuration II (discussed in the flow-field analysis section) are apparent on the pressures around the corner and just aft of the corner-cone junction. The overexpansion and subsequent separation of the flow on the corner creates a low pressure on the corner and extreme forward tip of the cone compared with the pressures rearward on the cone. This apparent separation phenomenon is not observed at $M = 9.6$ in figure 6. The pressure distributions of configuration I in figures 3 and 4 also do not indicate separation. As noted in the flow-field analysis section, if separation did occur on configuration I, it affected a much smaller region than on configuration II. Since there is less instrumentation in the corner region of configuration I than in that of configuration II, a small region of separation might not be seen in the pressure distributions.

Conical-cylindrical afterbody.- Comparison of experimental pressure distributions with the Newtonian theory in figures 3 to 6 shows that the pressures over the forward portion of the cone of each configuration are always larger than the Newtonian pressure. These high experimental pressures are induced by the strong bow shock wave caused by the very blunt nose shape of each configuration. In fact, the leeward surface pressures are larger than the Newtonian values over the entire cone surface, even when portions of the cone are in the Newtonian "shadow" region. On the windward side of the cones, the nose bluntness effects quickly die out with increasing values of s/r for $\alpha \leq 15^\circ$ so that the surface pressures over the rearward portion of the cone are either about equal or slightly less than the Newtonian pressures. For $\alpha > 15^\circ$, the windward surface pressures on the conical surface are higher than the theory over most of the cone, the deviation increasing as the angle of attack increases.

The surface pressures on the cylindrical afterbody (figs. 3 to 6) are generally in agreement with the theory through the angle-of-attack range and the Mach numbers investigated for each configuration. The experimental pressures on the cylindrical afterbody of configuration I are approximately the same as those on configuration II; thus, the nose-shape variation has no effect in this region.

Heat-Transfer Distributions

The heat-transfer distributions at both Mach number 6.0 and 9.6 are presented in figures 7 and 8 for configurations I and II, respectively, over the angle-of-attack range. The measured heat-transfer coefficients referenced to the theoretical stagnation heating rate of a hemisphere $h_{s,hemi}$ determined from a modification of the theory of Sibulkin are presented in dimensionless ratio form. (See ref. 6.) The heating rate at the stagnation point is given by

$$\frac{\frac{h_{s,hemi} D}{K_{\sigma}}}{\sqrt{\frac{\rho_{\sigma} u_{\sigma} D}{\mu_{\sigma}}}} = 0.763 N_{Pr, \sigma}^{0.4} \left(\frac{\beta D}{u_{\sigma}} \right)^{0.5} \quad (4)$$

where the velocity gradient parameter at the stagnation point $\frac{\beta D}{u_{\sigma}}$ was determined from modified Newtonian theory. The diameter of curvature of the spherical segment nose D was used for both configurations to calculate $h_{s,hemi}$.

It should be noted that at $M = 6.0$, the heat-transfer distribution over the leeward portion of the cone was not obtained for angles of attack above 10° . Also, at $M = 6.0$, the data for the rearward portion of the leeward cone region of configuration I(a) at $\alpha = 10^{\circ}$ and configuration II(a) at $\alpha = 5^{\circ}$ and 10° have been omitted because of interference effects caused by a disturbance emanating from the tunnel wall cavity (for model injection) and intersecting the conical portion of the model.

Finally, a model imperfection just aft of the 5.7° and 9° cone intersection on model II(a) was created during thermocouple installation. This protrusion on the $\phi = 90^{\circ}$ ray apparently affected the heating rates rearward of the cone intersection at certain angles of attack and Reynolds numbers by tripping the boundary layer and thereby causing transition and higher heating rates.

Data accuracy as affected by model size and test techniques.— The distributions of heating on the nose of both models I(a) and II(a) at $M = 6.0$ (figs. 7 and 8) show the maximum heating to be near the corner radius even at $\alpha = 0^{\circ}$. The comparable tests at $M = 9.6$ using the smaller models do not show a similar rise in the heating toward the edge radius even though theory gives a rise which is essentially independent of Mach number. Furthermore, just downstream of the corner radius, the heating distribution at $M = 6.0$ usually shows a small minimum (note particularly the windward ray) which is also not seen in the $M = 9.6$ distributions. These differences in results are attributed to the effects of

model size and testing techniques. The smaller size of the models tested at $M = 9.6$ and the larger time required to stabilize flow conditions lead to larger conduction errors. This is of particular importance in the region of small radius (hence, large heat-transfer gradients which result in large skin-temperature gradients) such as the corners and adjacent regions of configurations I and II. The shorter surface lengths and longer times involved in the $M = 9.6$ tests permitted the heat absorbed by the skin at the forward part of the corner to be conducted to the lower temperature skin just downstream of the corner. Hence, neither the peak heating ratio ahead of the corner nor the minimum just downstream of the corner seen in the $M = 6$ tests was detected in measuring the heat stored in the skin during the $M = 9.6$ tests. The increase in heating in the corner region above the stagnation level at $\alpha = 0^\circ$ is of importance and verifies the predictions of the theories of Lees (ref. 7), Beckwith and Cohen (ref. 8), and others for a body of this type.

Discussion.— The distributions presented in figures 7 and 8 indicate that the heat transfer in the region of the forward-most corner is always greater than the measured values at the $\alpha = 0$ geometric vertex regardless of angle-of-attack range for $M = 6$. The increase may be as much as 65 percent, depending on the angle of attack. This increase is also indicated for the $M = 9.6$ distributions at angles of attack $\geq 10^\circ$.

For configuration I(a) at $M = 6.0$, a slight separation region on the cone just beyond the corner at 0° angle of attack (fig. 7(a)) is indicated by the relatively low heating measured. For $\alpha > 0^\circ$ (figs. 7(b) to 7(f)), there is insufficient instrumentation to determine whether the flow separates over the windward ray. A separation region is not apparent in the $M = 9.6$ data for configuration I(b).

In figure 8(a), a possible separation region is indicated for configuration II(a) at $M = 6.0$. For $\alpha > 0^\circ$ (figs. 8(b) to 8(f)), the separation region is always evident on the horizontal ray. On the windward ray, the flow also might be separated up to an angle of attack of 15° . However, the heat-transfer coefficient is higher than might be expected for a separated region. Perhaps this is due to conduction. No comparable decrease in heating is seen in the corner region for the $M = 9.6$ data of configuration II(b).

It is felt that the increase in heating rates over the rearward portion of the cone on the windward ray for the $M = 6.0$ distributions (on configuration II(a) in fig. 8) is the effect of boundary-layer transition which may have been influenced by the protrusion in the model skin previously mentioned. At $\alpha = 30^\circ$, natural transition may also have occurred. (See fig. 7(f).)

An unusual trend is apparent in the distributions for configurations I(b) and II(b) at $M = 9.6$. (See figs. 7(e) and 8(e).) The heat transfer over the leeward (vertical) ray begins to increase for a s/r value of approximately -3.0 and increases by 500 percent. This unusual phenomenon is unexplained.

For comparison, the heating rates on the windward ray of the cone are predicted by a simple crossflow theory where the cone is considered to be a cylinder swept to an angle equal to the local surface inclination and having a

radius equal to the local cone radius. A prediction of the heating rate can be obtained from the results of references 9 and 10 as

$$\frac{h}{h_{s, \text{hemi}}} = \frac{0.57}{0.76} \sqrt{\frac{r_{\text{hemi}}}{r_l}} \cos(90 - \alpha - \delta) \quad (5)$$

This prediction is presented for the highest angles of attack, 25° and 30° , in figures 7(e), 7(f), 8(e), and 8(f). The agreement of this theory with the measured heating was extremely good, a result that was not expected when the short length of the body was considered.

Mach number and Reynolds number effects at $\alpha = 0^\circ$. Figure 9 presents the measured heat-transfer distribution referenced to the theoretical stagnation heating on a hemisphere over the full Reynolds number range at an angle of attack of 0° . The increase of Mach number from 6.0 to 9.6 and the concurrent decrease in Reynolds number by a factor of 10 did not significantly affect the laminar heat transfer for the configurations tested through an angle-of-attack range of 0° to 25° . There is seen to be little uniform effect on the heating rates except in the corner region and over the rear portion of the cone. The deviation of heating rates in the corner region between models I(a) and I(b) or models II(a) and II(b) at $M = 6$ indicate that the conduction error in a region of small radius is mainly due to the smaller model size since the testing technique is the same for all the $M = 6.0$ tests. Evidence is given that the conduction error may also wash out the apparent separation effect since the smaller models do not indicate the effects of separation on heat transfer as do the larger models. However, it should be noted that this may very well be an effect of Reynolds number variation since there are no schlieren photographs available to confirm the existence of separation on the smaller models.

The variation in heating over the rearward portion of the cone may be due to a Reynolds number effect connected with the beginning of transition. Certainly this is evident for configuration II (fig. 9(b), $R_r = 0.93 \times 10^6$) where for the maximum Reynolds number the boundary layer is definitely transitional.

In reference 11 the effect of having a spherical segment nose rather than a full hemisphere is shown to increase the stagnation velocity gradient and hence stagnation-point heating above the hemisphere stagnation level. In figure 10, the measured stagnation heating rates are compared with the heat-transfer rate by using the velocity gradient of Boison and Curtiss in reference 11. Using the Boison-Curtiss correlation as a reference, the variation of the measured stagnation-heating-rate ratio is generally less than 10 percent for each configuration over the Reynolds number range (in which R_r is varied by a factor of 12 times the minimum value obtained in the $M = 9.6$ tests). Since this variation agrees with the accuracy which was expected in these tests, it may be said that Reynolds number had no effect on the stagnation-heating parameter $h/h_{s, \text{hemi}}$.

Comparison of heat-transfer distribution with theory at $\alpha = 0^\circ$. Figure 11 presents the measured heat-transfer distributions referenced to the measured stagnation heating rate for the full range of Reynolds number. Also presented

in figure 11 are the theoretical heat-transfer distributions as predicted by the theory of Lees (ref. 7).

Calculations have been based on a Newtonian pressure distribution for $M = 6.0$ and $M = 9.6$ and measured pressure distribution for $M = 6.0$. The theory agrees reasonably well with the experimental values over the nose surface up to the corner region for each configuration, as might be expected. The rise in heating on the corner region is less than that predicted by theory. However, even for the $M = 6$ tests there must be some conduction error in the corner region so that it is reasonable to postulate that more accurate experimental data (less conduction) should give better agreement than the results indicate. Over the conical-cylindrical afterbody, the theory gives a reasonable prediction in the trends of the data. However, the theory neglects the effects of pressure gradient on boundary-layer profiles and is expected to be higher than experiment. Hence, the theory is applied here only to give qualitative results and is not intended to give an accurate prediction in this region. The theoretical distribution based on the measured pressure distribution gives the best estimate of the trends of the data. It is evident that a change in pressure distribution (that is, between measured and Newtonian values) can give a marked variation in theoretical predictions. Note that the theory (using a Newtonian pressure distribution) predicts a much larger increase in heating at the 5.7° to 9° cone junction of configuration II (fig. 11(b)) than was found in any of the tests.

SUMMARY OF RESULTS

Heat-transfer and pressure distributions have been obtained for two reentry configurations for the five-stage Scout vehicle over an angle-of-attack range of 0° to 30° in the Langley 20-inch Mach 6 tunnel and 0° to 25° in the Mach number 9.6 nozzle of the Langley 11-inch hypersonic tunnel. Analysis of the experimental data and comparison with theory have yielded the following results:

1. Modified Newtonian theory gives a good prediction of the trends of the pressure distributions through the angle-of-attack range.
2. Heat-transfer data accuracy is strongly affected by model size and testing techniques particularly in a region of large gradients of heat transfer (corner region). Experimentally, the heat-transfer peak on the corner can be lost because of conduction.
3. The heating rates on the corner region of the configurations tested are greater than the measured values at the $\alpha = 0$ geometric vertex regardless of angle of attack within the range investigated for $M = 6$. The increase may be as much as 65 percent depending upon the angle of attack.
4. The increase of Mach number of 6.0 to 9.6 and the concurrent decrease in Reynolds number by a factor of 10 did not significantly affect the laminar heat-transfer distribution over the configurations tested through an angle-of-attack range of 0° to 25° .

5. At the high angles of attack (25° and 30°) for which the low-angle conical afterbody may be approximated by a cylinder, crossflow theory was found to predict the measured heating level on the windward ray extremely well.

6. The variation of free-stream Reynolds number by a factor of 12 had no significant effect on either the stagnation heating ratio or the heat-transfer distributions at an angle of attack of 0° where the flow was laminar.

7. The correlation of Boison and Curtiss for the effect of having a spherical segment nose rather than a full hemispherical nose on the stagnation heating agrees well with the experimental results.

8. The theory of Lees agrees reasonably well with the experimental results over the nose of the configurations. On the conical afterbody, Lees theory is higher than the measured heating rates.

Langley Research Center,
National Aeronautics and Space Administration,
Langley Station, Hampton, Va., February 18, 1963.

REFERENCES

1. Mayhue, Robert J., Compiler: NASA Scout ST-1 Flight-Test Results and Analyses, Launch Operations, and Test Vehicle Description. NASA TN D-1240, 1962.
2. Johnston, Patrick J.: Longitudinal Aerodynamic Characteristics of Several Fifth-Stage Scout Reentry Vehicles From Mach Number 0.60 to 24.4 Including Some Reynolds Number Effects on Stability at Hypersonic Speeds. NASA TN D-1638, 1963.
3. Harrison, Edwin F.: Static Stability Tests in the Langley 24-Inch Hypersonic Arc Tunnel on a Blunted Cone at a Mach Number of 20. NASA TN D-1508, 1962.
4. Sterrett, James R., and Emery, James C.: Extension of Boundary-Layer-Separation Criteria to a Mach Number of 6.5 by Utilizing Flat Plates With Forward-Facing Steps. NASA TN D-618, 1960.
5. Bertram, Mitchel H.: Boundary-Layer Displacement Effects in Air at Mach Numbers of 6.8 and 9.6. NASA TR R-22, 1959. (Supersedes NACA TN 4133.)
6. Crawford, Davis H., and McCauley, William D.: Investigation of the Laminar Aerodynamic Heat-Transfer Characteristics of a Hemisphere-Cylinder in the Langley 11-Inch Hypersonic Tunnel at a Mach Number of 6.8. NACA Rep. 1323, 1957. (Supersedes NACA TN 3706.)
7. Lees, Lester: Laminar Heat Transfer Over Blunt-Nosed Bodies at Hypersonic Flight Speeds. Jet Propulsion, vol. 26, no. 4, Apr. 1956, pp. 259-269, 274.
8. Beckwith, Ivan E., and Cohen, Nathaniel B.: Application of Similar Solutions to Calculation of Laminar Heat Transfer on Bodies With Yaw and Large Pressure Gradient in High-Speed Flow. NASA TN D-625, 1961.
9. Truitt, Robert Wesley: Fundamentals of Aerodynamic Heating. The Ronald Press Co., c.1960.
10. Feller, William V.: Investigation of Equilibrium Temperatures and Average Laminar Heat-Transfer Coefficients for the Front Half of Swept Circular Cylinders at a Mach Number of 6.9. NACA RM L55F08a, 1955.
11. Boison, J. Christopher, and Curtiss, Howard A.: An Experimental Investigation of Blunt Body Stagnation Point Velocity Gradient. ARS Jour., vol. 29, no. 2, Feb. 1959, pp. 130-135.

TABLE I.- COORDINATES OF THERMOCOUPLES AND PRESSURE ORIFICES

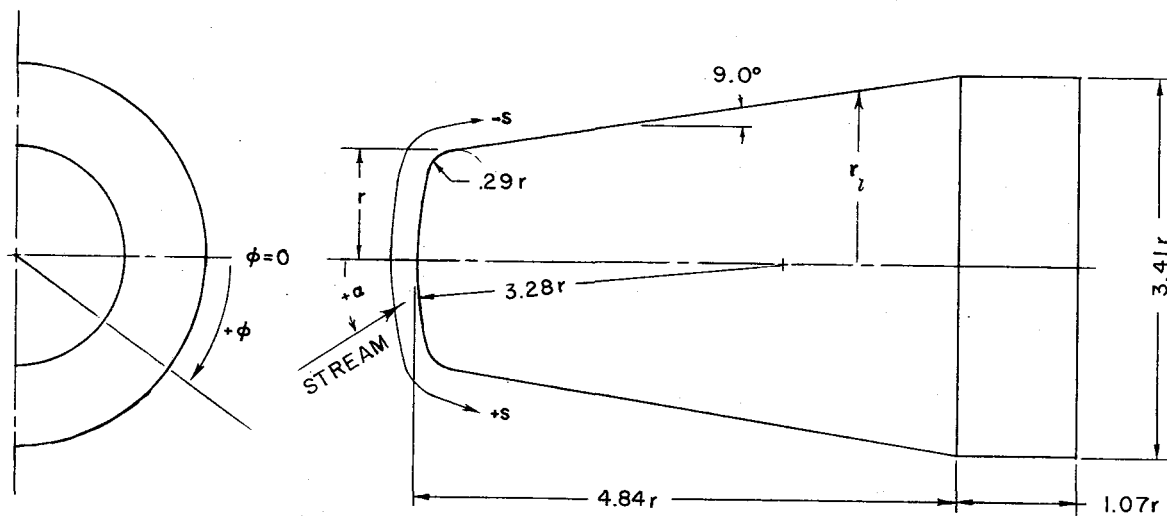
(a) Configuration I

Coordinates				Skin thickness, t , in., for heat-transfer model -		Instrumentation for -			
						Heat-transfer model		Pressure model	
s/r	x/r	ϕ , deg	r_l/r	I(a)	I(b)	I(a)	I(b)	I(a)	I(b)
0	-----	---	0	0.049	0.053	X	X	X	X
.229	-----	0	.229	.050	.053	X	X	X	
.229	-----	90	.229	.050	.053	X	X	X	X
.459	-----	0	.456	.050	.050	X	X	X	
.459	-----	90	.456	.050	.050	X	X	X	X
.687	-----	0	.681	.049	.046	X	X	X	X
.687	-----	30	.681	.049	.046	X	X	X	X
.687	-----	60	.681	.050	.047	X	X	X	X
.687	-----	90	.681	.049	.046	X	X	X	X
.847	-----	90	.839	.043	.043	X	X		
.928	-----	90	.920					X	X
.950	-----	0	.940	.045	.040	X	X	X	X
1.071	0.246	90	-----	.031	.028	X	X		
1.166	.341	0	-----	.031	.028	X	X	X	
1.166	.341	30	-----	.032	.026	X	X	X	
1.166	.341	60	-----	.032	.026	X	X	X	
1.166	.341	90	-----	.036	.039	X	X	X	X
1.304	.478	0	-----	.029	.031	X	X	X	
1.434	.627	0	-----					X	X
1.434	.627	90	-----					X	X
1.705	.873	90	-----	.030	.030	X	X		
1.914	1.104	0	-----	.031	.030	X	X	X	X
1.914	1.104	165	-----	.030	.031	X	X		
1.914	1.104	150	-----	.030	.031	X	X	X	X
1.914	1.104	135	-----	.030	.031	X	X		
1.914	1.104	120	-----	.030	.031	X	X	X	X
1.914	1.104	105	-----	.030	.031	X	X		
1.914	1.104	90	-----	.030	.031	X	X	X	X
2.424	1.582	90	-----	.029	.031	X	X		
2.908	2.060	0	-----	.029	.031	X	X	X	
2.908	2.060	90	-----	.029	.031	X	X	X	X
3.336	2.480	90	-----	.030	.031	X	X		
3.881	2.882	0	-----	.032	.034	X	X	X	X
3.881	2.882	165	-----	.032	.032	X	X		
3.881	2.882	150	-----	.032	.032	X	X	X	X
3.881	2.882	135	-----	.032	.032	X	X		
3.881	2.882	120	-----	.032	.032	X	X	X	X
3.881	2.882	105	-----	.032	.031	X	X		
3.881	2.882	90	-----	.030	.031	X	X	X	X
4.373	3.503	90	-----	.030	.031	X	X	X	
4.866	3.983	0	-----	.032	.032	X	X	X	
4.866	3.983	90	-----	.032	.034	X	X	X	X
5.225	4.487	90	-----	.032	.032	X	X	X	X
6.078	5.186	0	-----	.029	.032	X	X	X	
6.078	5.186	90	-----	.030	.033	X	X	X	X

TABLE I.- COORDINATES OF THERMOCOUPLES AND PRESSURE ORIFICES - Concluded

(b) Configuration II

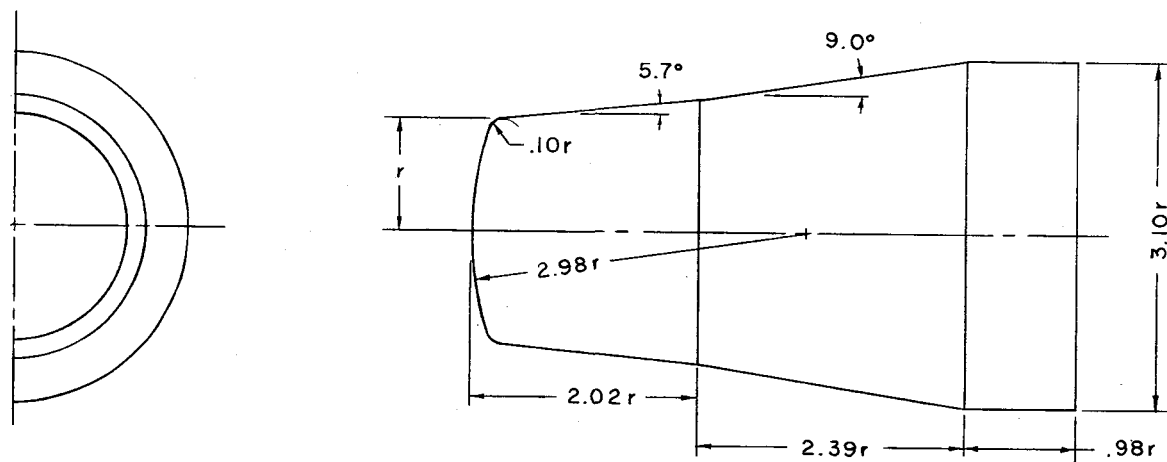
Coordinates				Skin thickness, t, in., for heat-transfer model -		Instrumentation for -			
s/r	x/r	ϕ , deg	r_2/r	II(a)	II(b)	Heat-transfer model		Pressure model	
0	0	---	0	0.051	0.051	X	X	X	X
.311	----	0	.310	.051	.051	X	X	X	X
.311	----	45	.310	.051	.051	X	X	X	
.311	----	90	.310	.051	.051	X	X	X	X
.468	----	90	.465					X	
.623	----	0	.618	.051	.050	X	X	X	X
.623	----	30	.618	.051	.050	X	X	X	
.623	----	60	.618	.051	.050	X	X	X	
.623	----	90	.618	.051	.050	X	X	X	X
.778	----	90	.770					X	
.933	----	0	.919	.046	.047	X	X	X	X
.933	----	15	.919	.046	.047	X	X	X	
.933	----	30	.919	.046	.047	X	X	X	X
.933	----	45	.919	.046	.047	X	X	X	
.933	----	60	.919	.046	.047	X	X	X	X
.933	----	75	.919	.046	.047	X	X	X	
.933	----	90	.919	.046	.046	X	X	X	X
.977	----	0	.962	.043	.037	X	X		
.977	----	90	.962	.043	.042	X	X		
1.075	.248	90	----	.032	.032	X	X	X	X
1.328	.501	0	----	.030	.033	X	X	X	X
1.328	.501	90	----	.029	.033	X	X	X	X
1.583	.749	0	----	.032	.031	X	X	X	
1.583	.749	90	----	.032	.033	X	X	X	X
2.085	1.251	0	----	.032	.030	X	X	X	X
2.085	1.251	165	----	.032	.032	X	X	X	
2.085	1.251	150	----	.032	.032	X	X	X	X
2.085	1.251	135	----	.032	.032	X	X	X	
2.085	1.251	120	----	.032	.032	X	X	X	X
2.085	1.251	105	----	.032	.031	X	X	X	
2.085	1.251	90	----	.032	.031	X	X	X	X
2.580	1.750	90	----	.034	.032	X	X	X	
3.080	2.242	0	----	.033	.032	X	X	X	
3.080	2.242	90	----	.033	.032	X	X	X	X
3.594	2.753	90	----	.032	.033	X	X	X	
4.089	3.235	0	----	.031	.032	X	X	X	X
4.089	3.235	165	----	.030	.032	X	X	X	
4.089	3.235	150	----	.030	.033	X	X	X	X
4.089	3.235	135	----	.030	.032	X	X	X	
4.089	3.235	120	----	.030	.032	X	X	X	X
4.089	3.235	105	----	.030	.033	X	X	X	
4.089	3.235	90	----	.030	.033	X	X	X	X
4.612	3.740	90	----	.032	.032	X	X	X	
5.112	4.248	90	----	.031	.032	X	X	X	
5.581	4.706	0	----	.030	.029	X	X	X	X
5.581	4.706	90	----	.031	.030	X	X	X	X



MODEL I(a) $r = 1.466$ inches

MODEL I(b) $r = .733$ inches

(a) Model I.

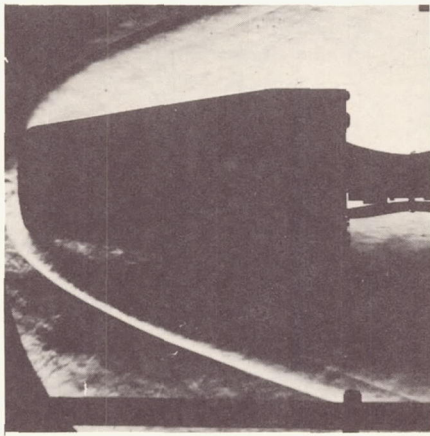


MODEL II (a) $r = 1.614$ inches

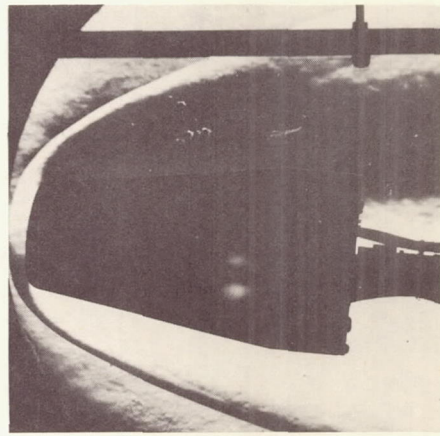
MODEL II(b) $r = .807$ inches

(b) Model II.

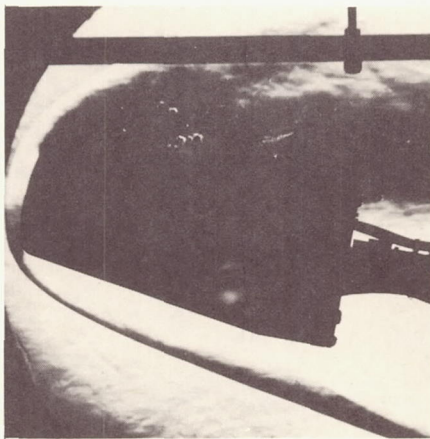
Figure 1.- Model dimensions.



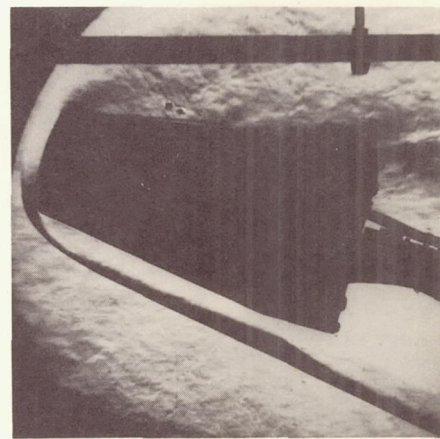
$\alpha = 0^\circ$



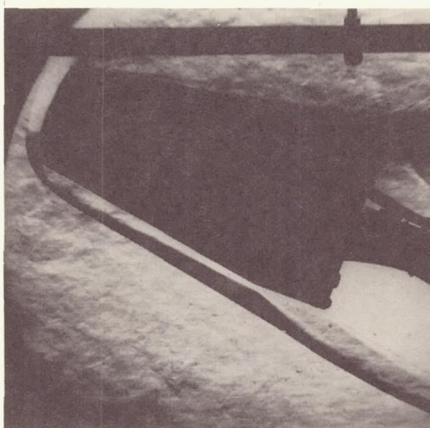
$\alpha = 5^\circ$



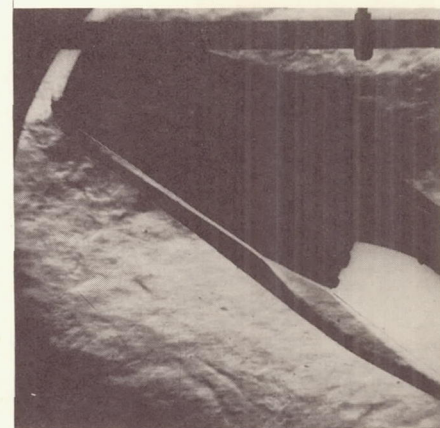
$\alpha = 10^\circ$



$\alpha = 15^\circ$



$\alpha = 20^\circ$

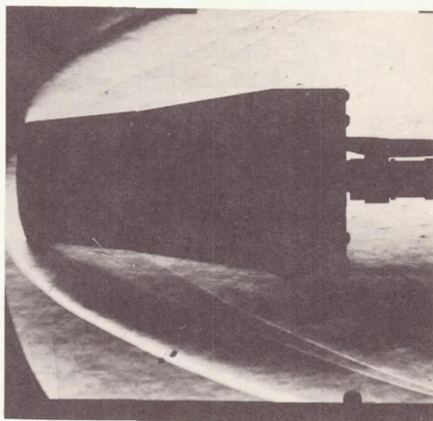


$\alpha = 25^\circ$

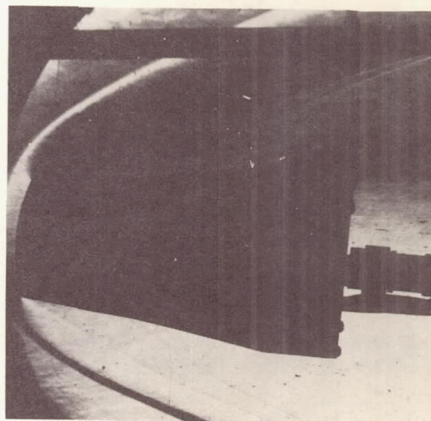
(a) Configuration I at $M = 6.0$.

L-63-55

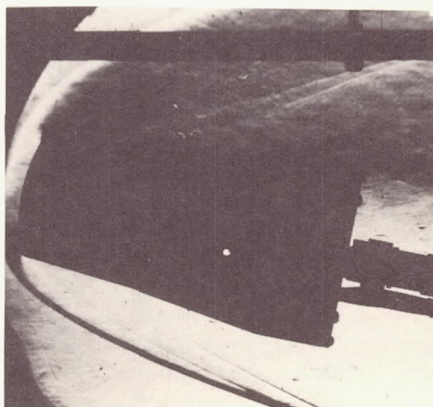
Figure 2.- Schlieren photographs.



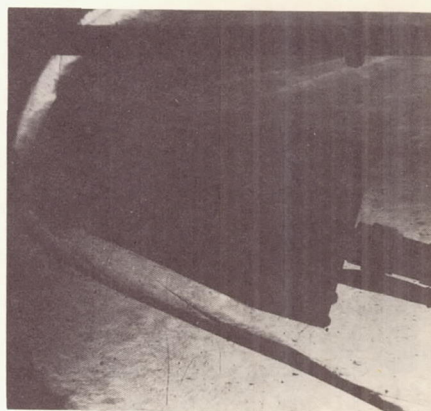
$\alpha = 0^\circ$



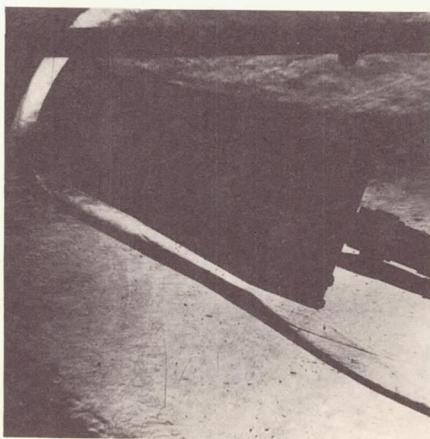
$\alpha = 5^\circ$



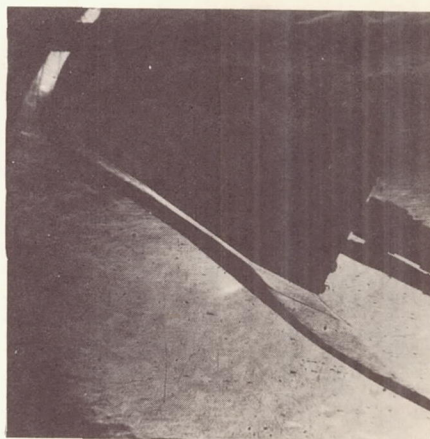
$\alpha = 10^\circ$



$\alpha = 15^\circ$



$\alpha = 20^\circ$

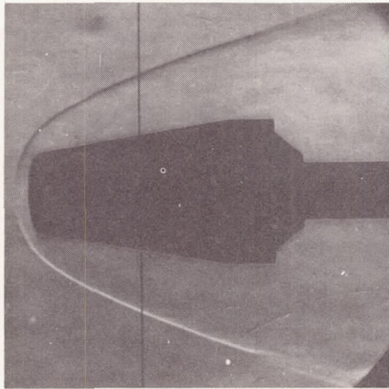


$\alpha = 25^\circ$

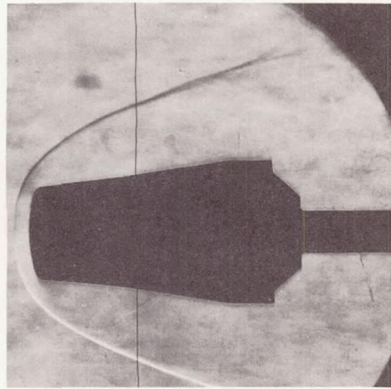
(b) Configuration II at $M = 6.0$.

L-63-56

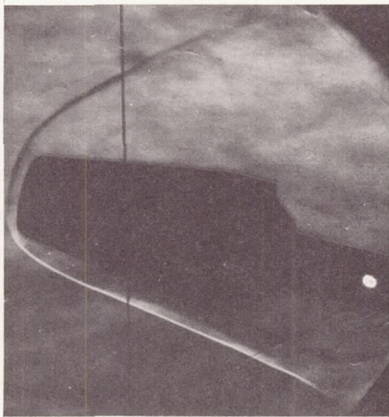
Figure 2.- Continued.



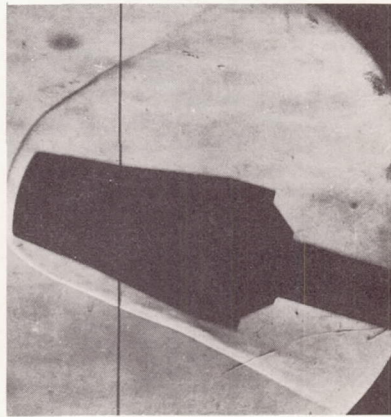
$\alpha = 0^\circ$



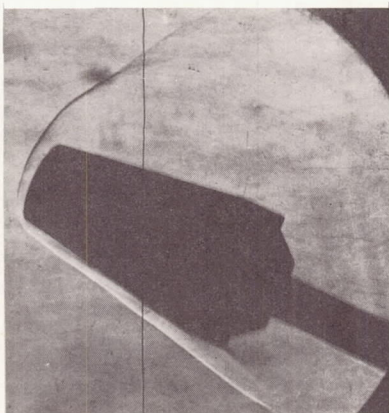
$\alpha = 0^\circ$



$\alpha = 15^\circ$

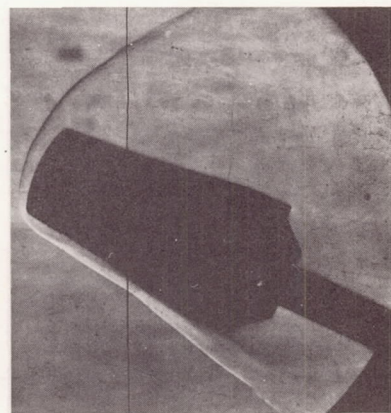


$\alpha = 15^\circ$



$\alpha = 25^\circ$

Configuration I



$\alpha = 25^\circ$

Configuration II

(c) $M = 9.6$.

L-63-57

Figure 2.- Concluded.



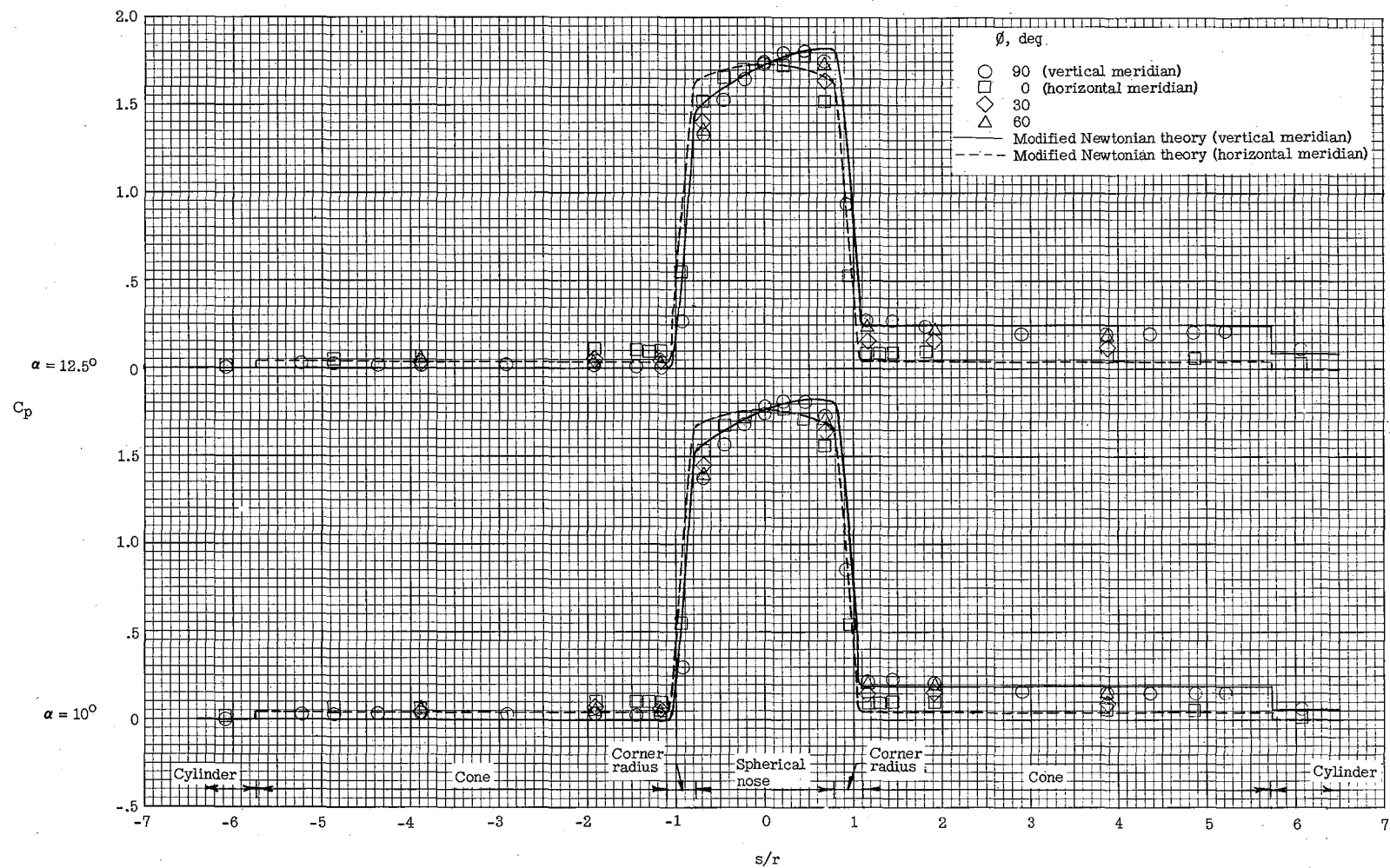
(a) $\alpha = 0^\circ$ and 2.5° .

Figure 3.- Pressure distribution over blunt-nose cone at $M = 6.0$. Configuration I(a).



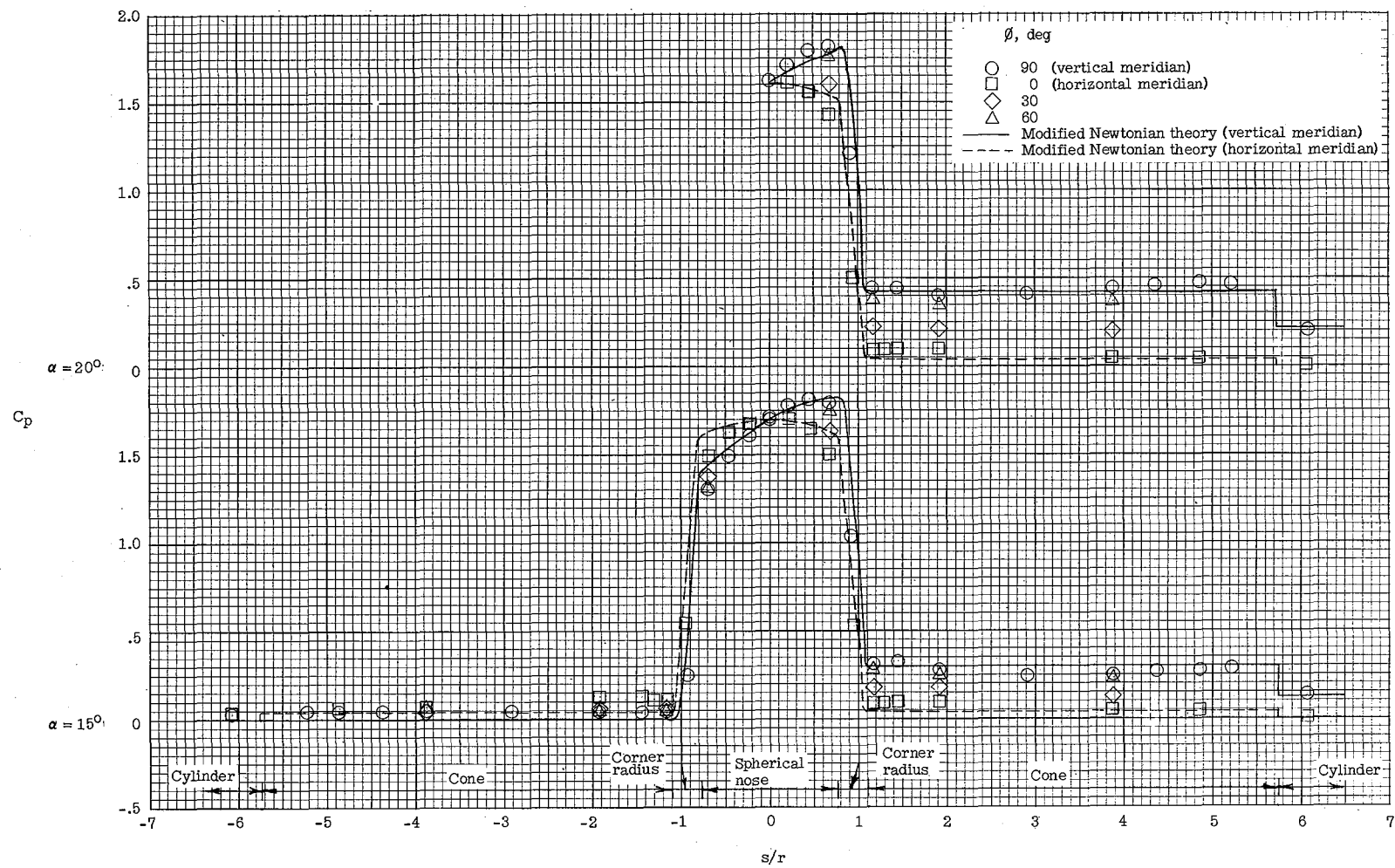
(b) $\alpha = 5^\circ$ and 7.5° .

Figure 3.- Continued.



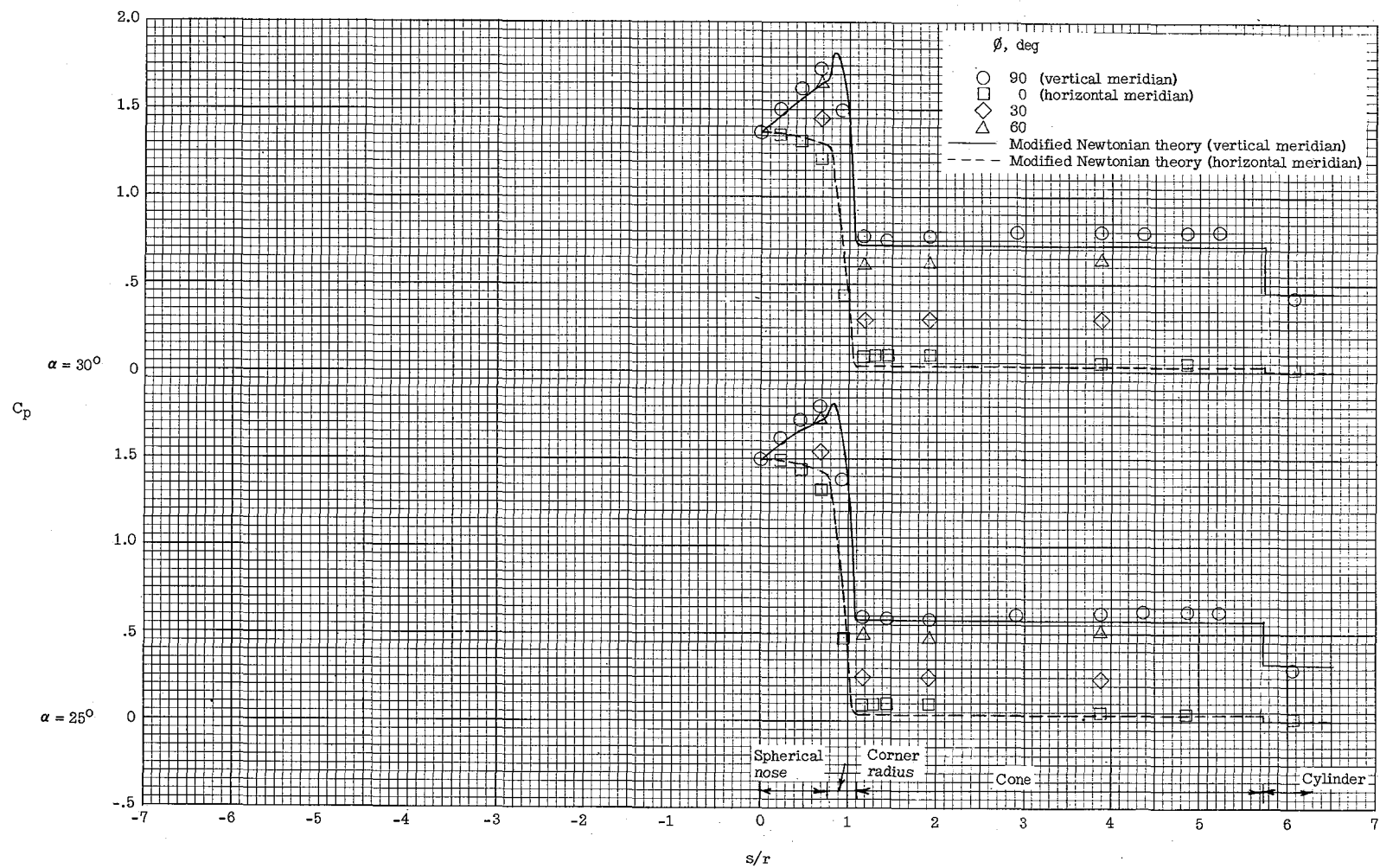
(c) $\alpha = 10^\circ$ and 12.5° .

Figure 3.- Continued.



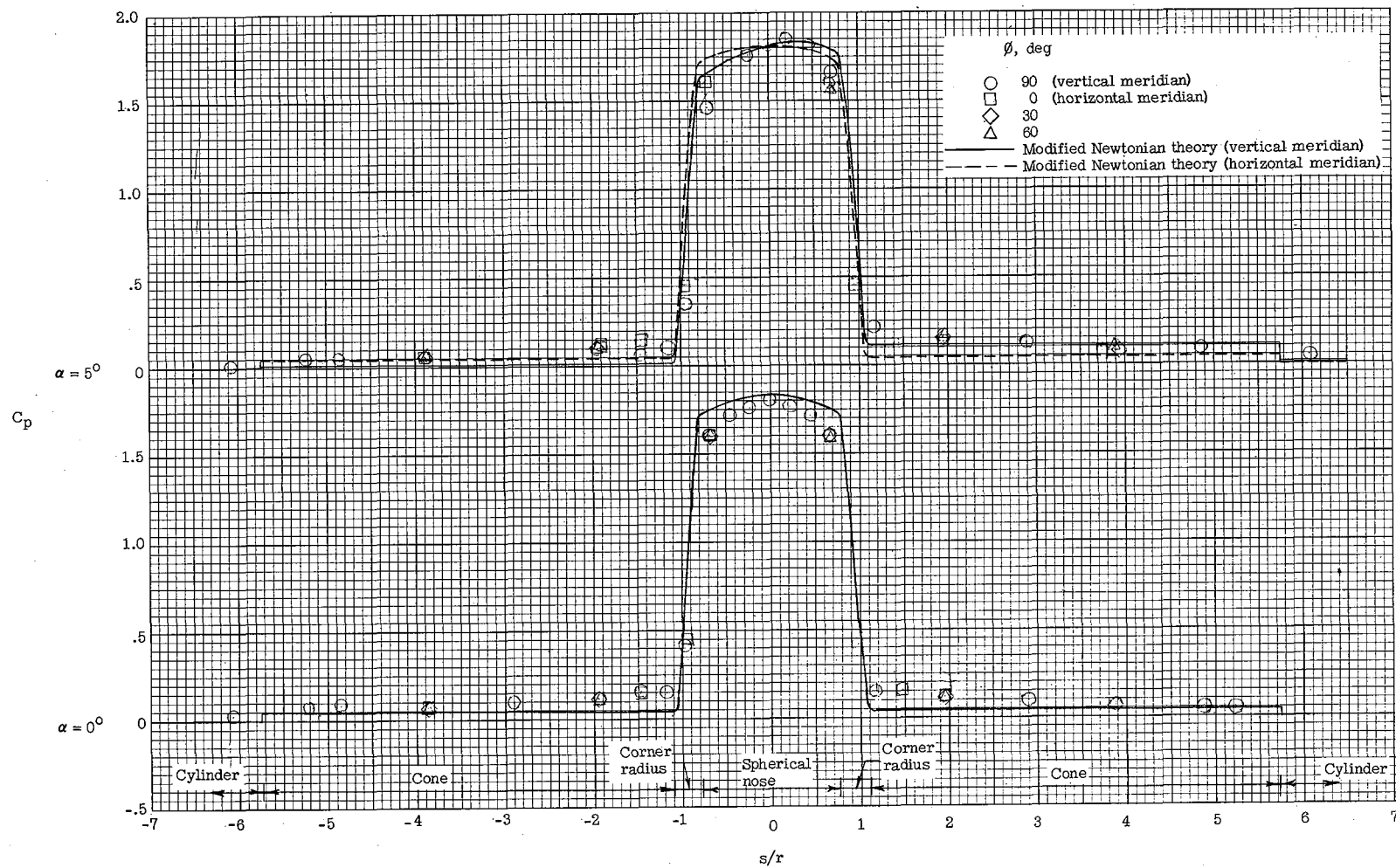
(d) $\alpha = 15^\circ$ and 20° .

Figure 3.- Continued.



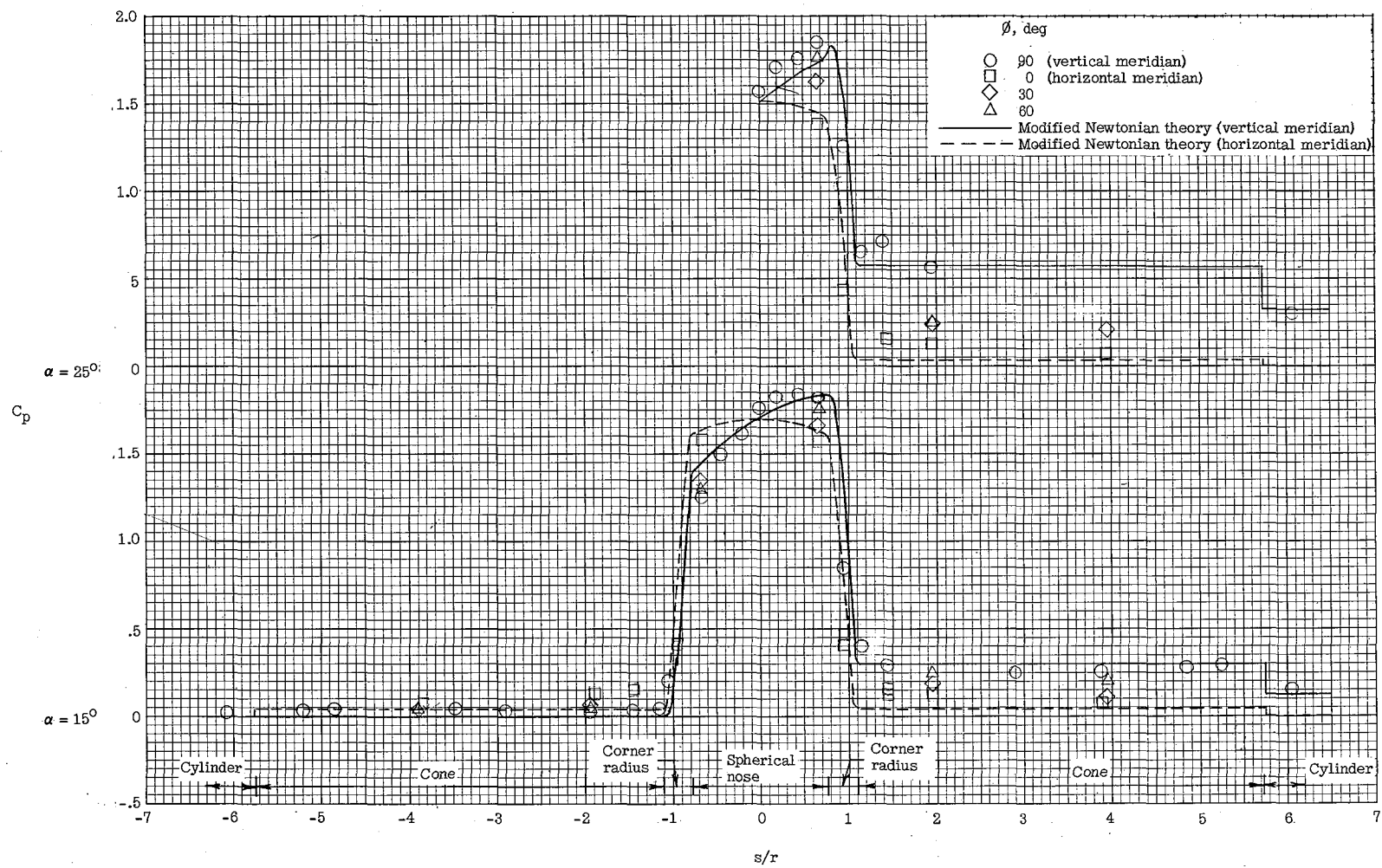
(e) $\alpha = 25^\circ$ and 30° .

Figure 3.- Concluded.



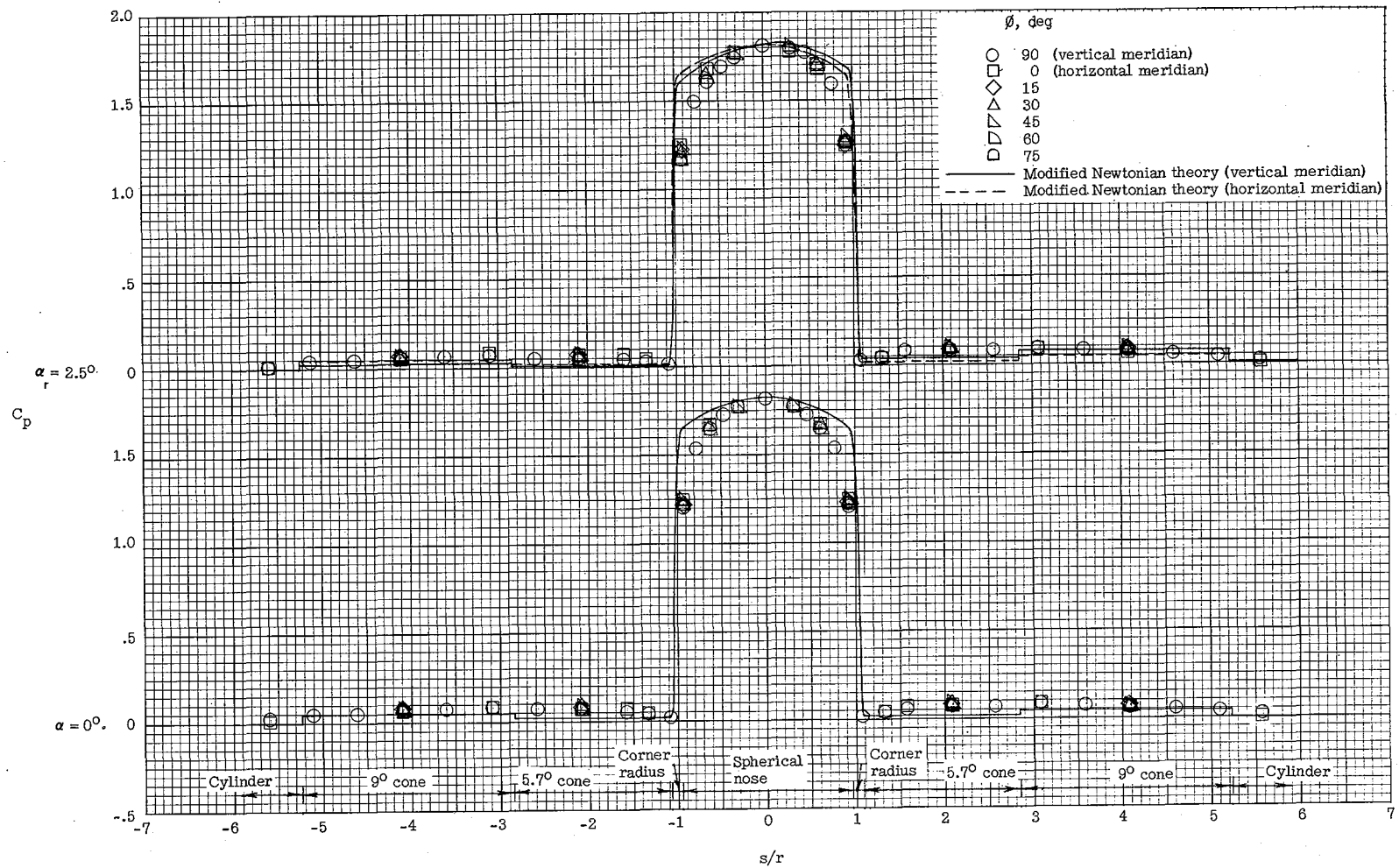
(a) $\alpha = 0^\circ$ and 5° .

Figure 4.- Pressure distribution over blunt-nose cone at $M = 9.6$. Configuration I(b).



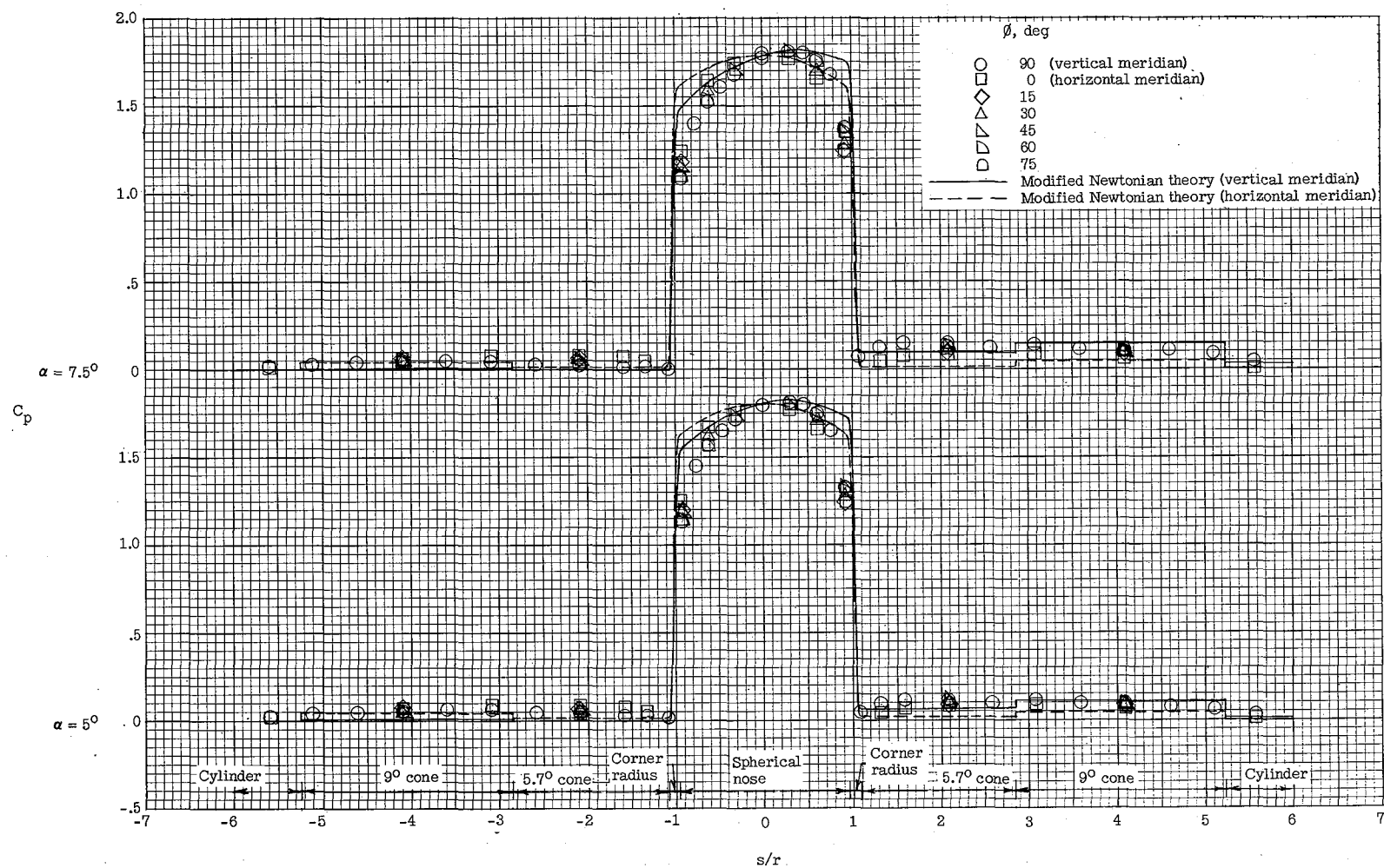
(b) $\alpha = 15^\circ$ and 25° .

Figure 4.- Concluded.



(a) $\alpha = 0^\circ$ and 2.5° .

Figure 5.- Pressure distribution over blunt-nose cone at $M = 6.0$. Configuration II(a).



(b) $\alpha = 5^\circ$ and 7.5° .

Figure 5.- Continued.

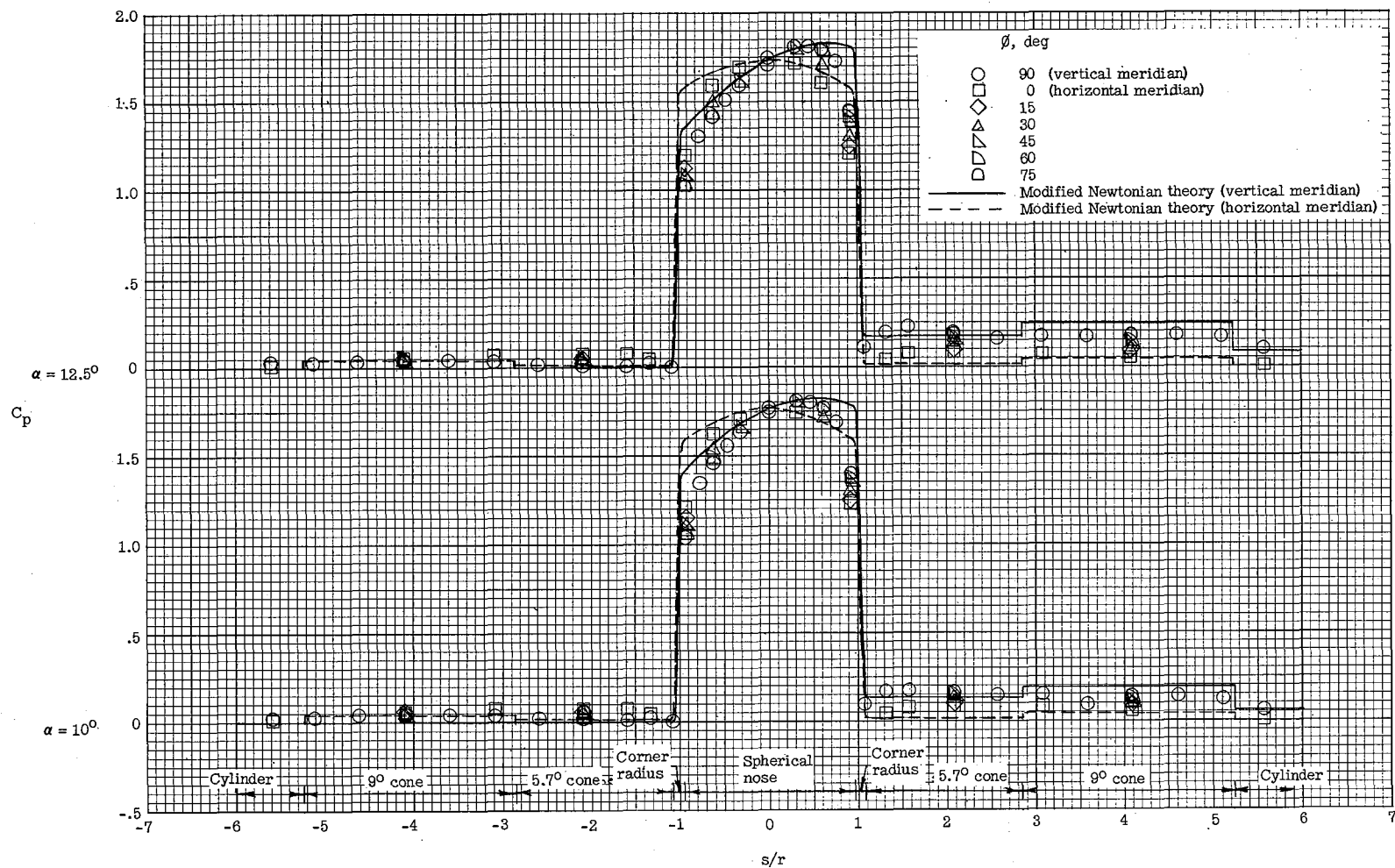
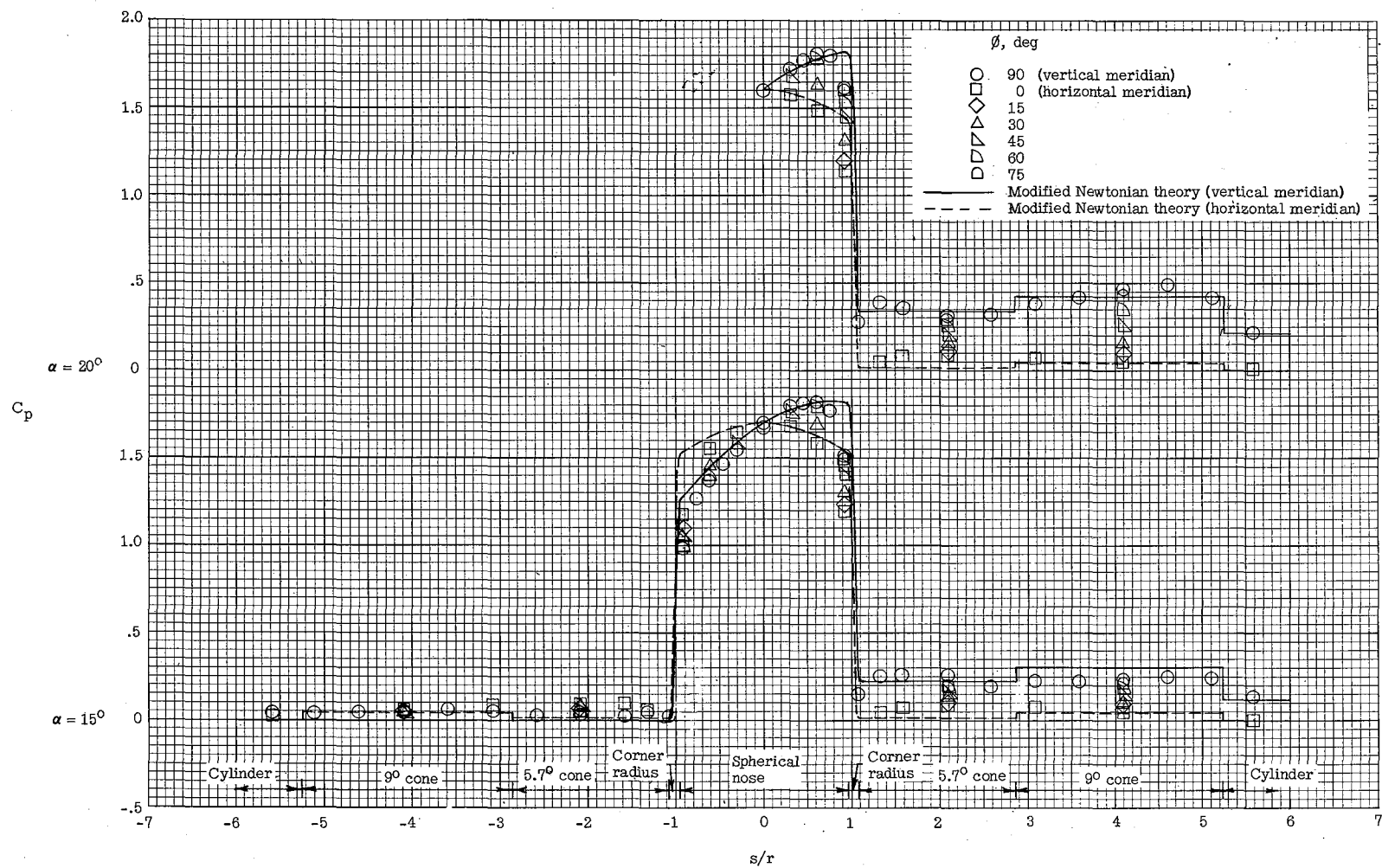
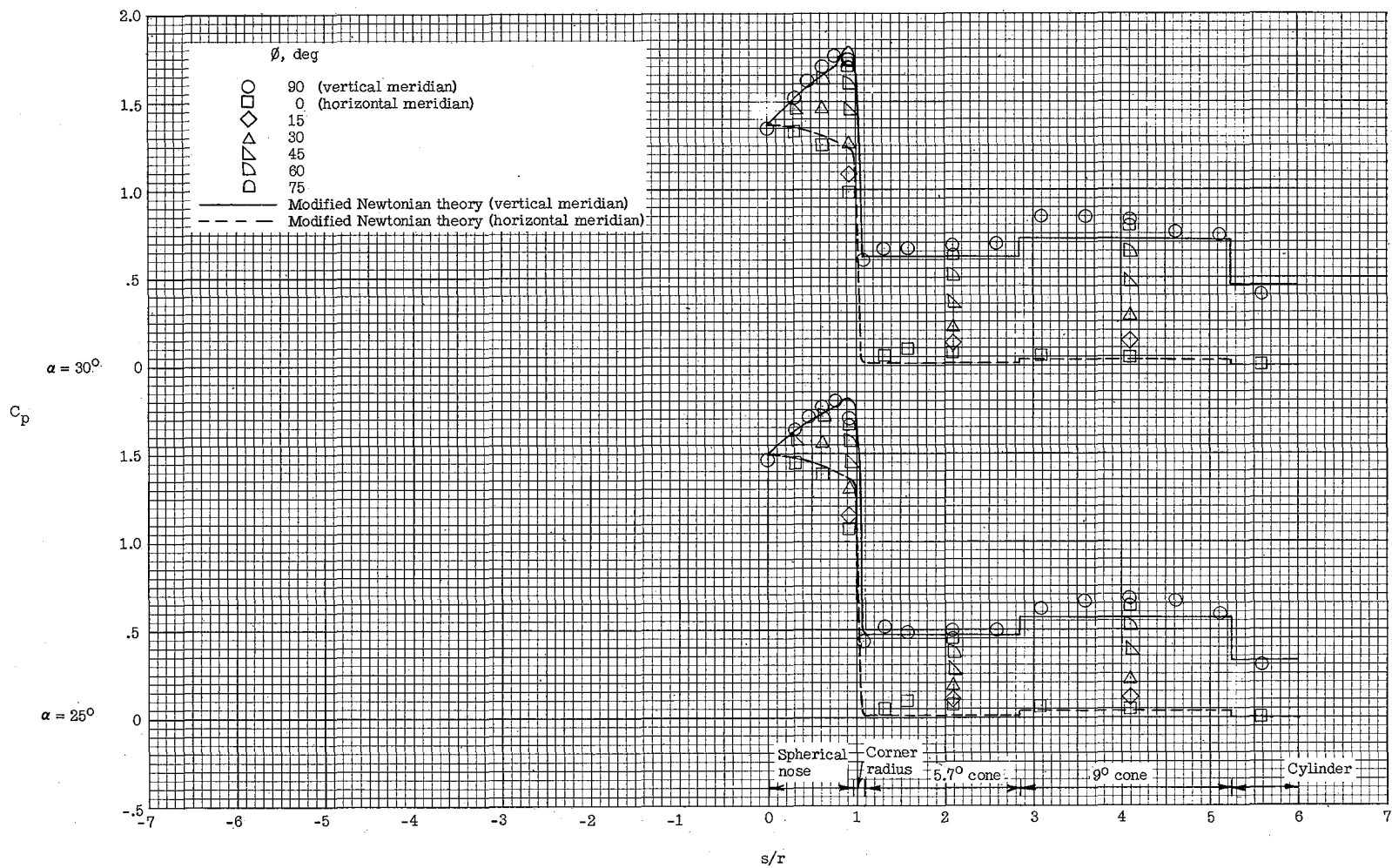
(c) $\alpha = 10^\circ$ and 12.5° .

Figure 5.- Continued.



(d) $\alpha = 15^\circ$ and 20° .

Figure 5.- Continued.



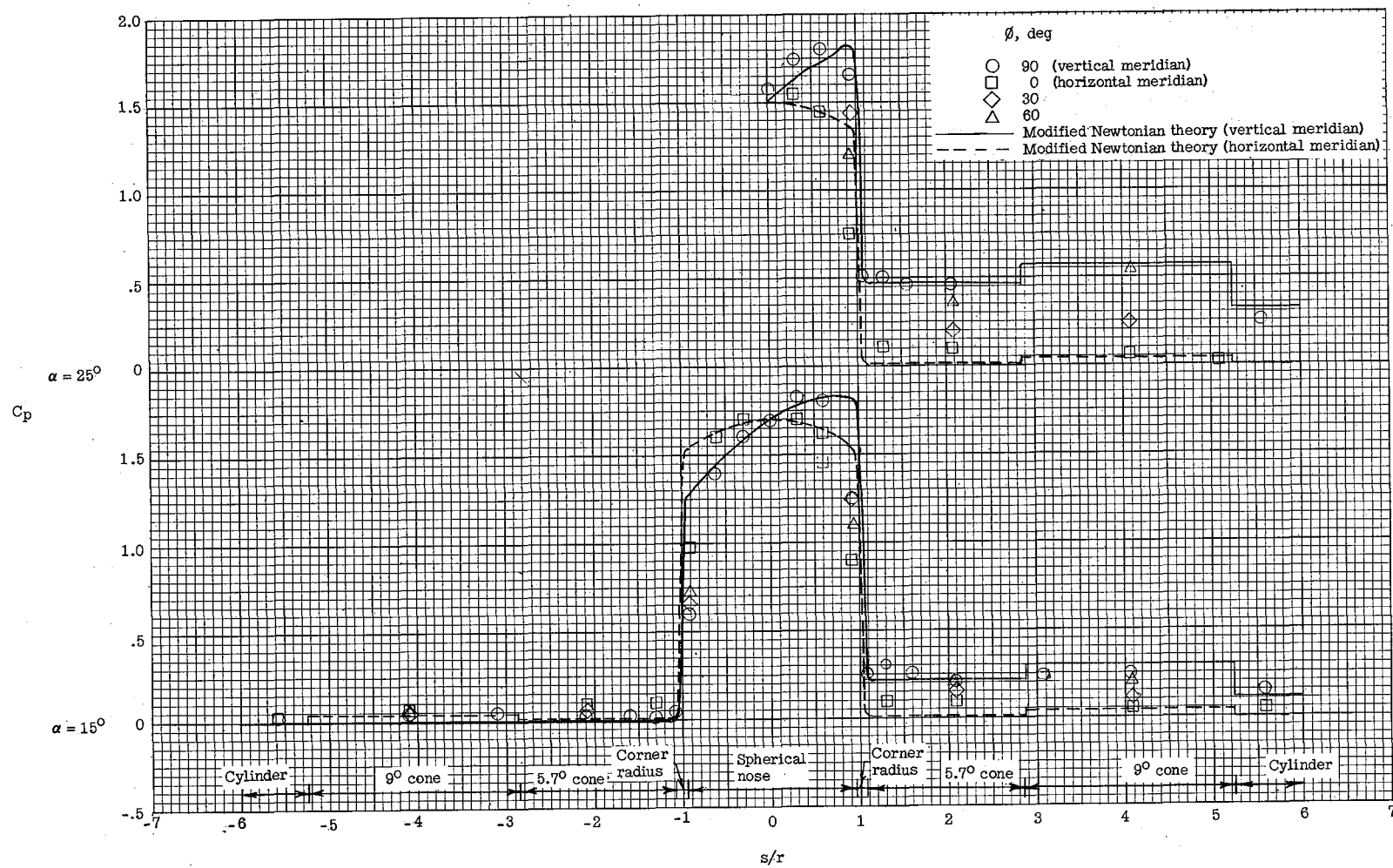
(e) $\alpha = 25^\circ$ and 30° .

Figure 5.- Concluded.



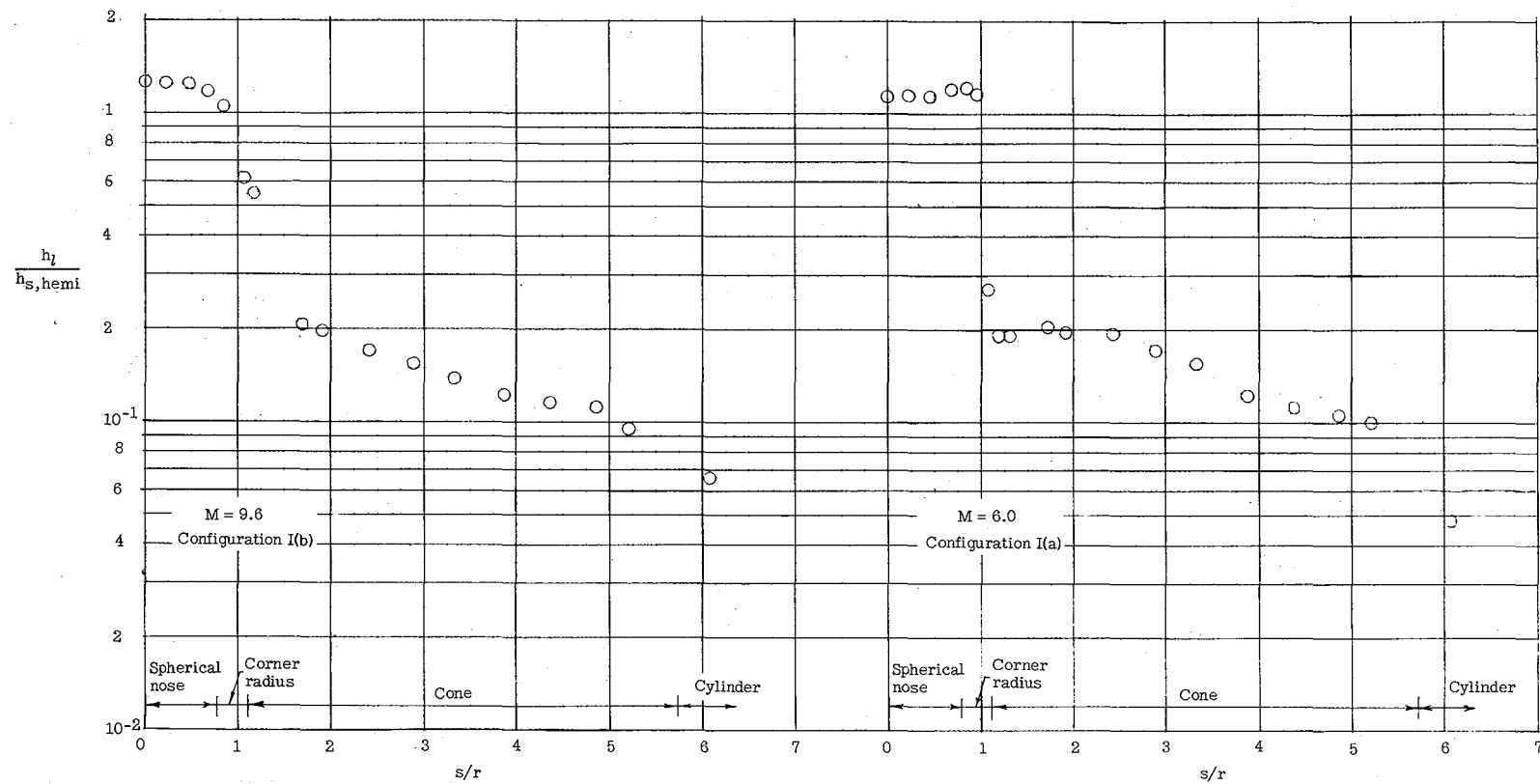
(a) $\alpha = 0^\circ$ and 5° .

Figure 6.- Pressure distribution over blunt-nose cone at $M = 9.6$. Configuration II(b).



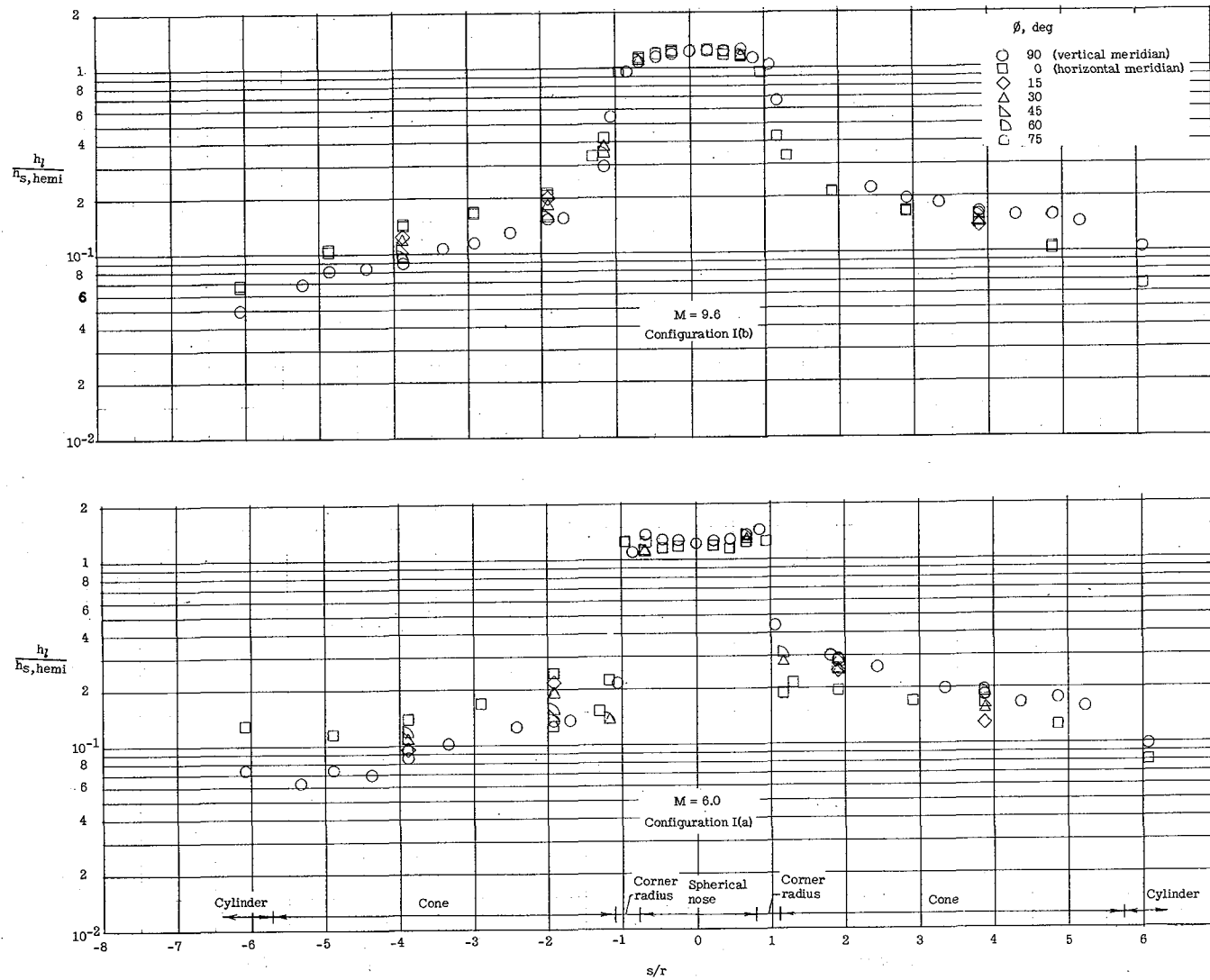
(b) $\alpha = 15^\circ$ and 25° .

Figure 6.- Concluded.



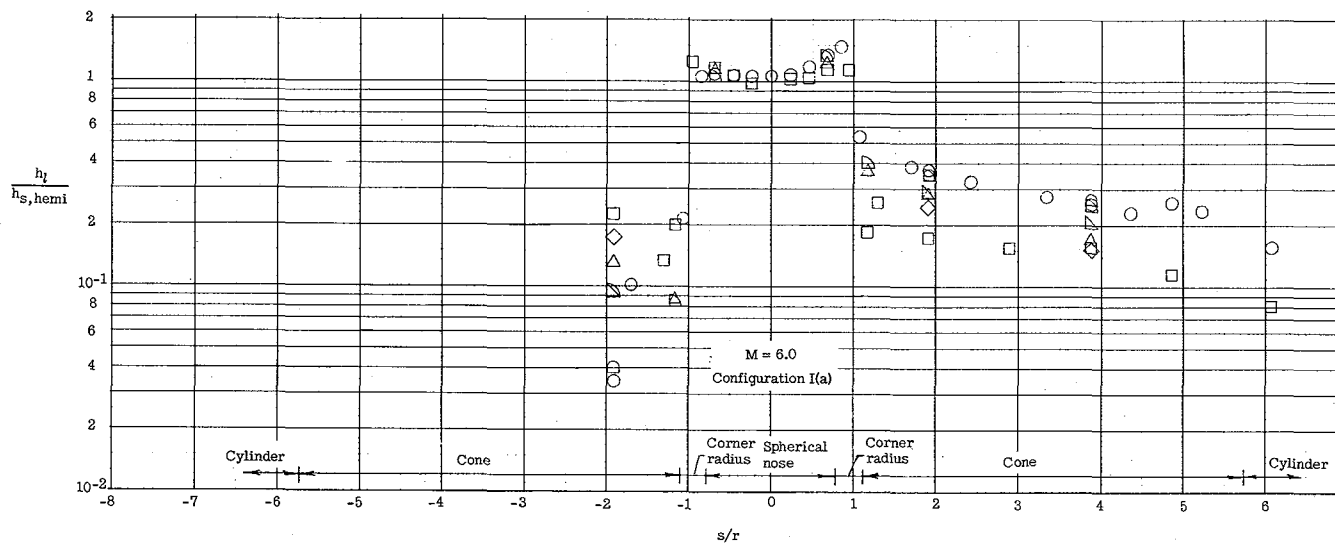
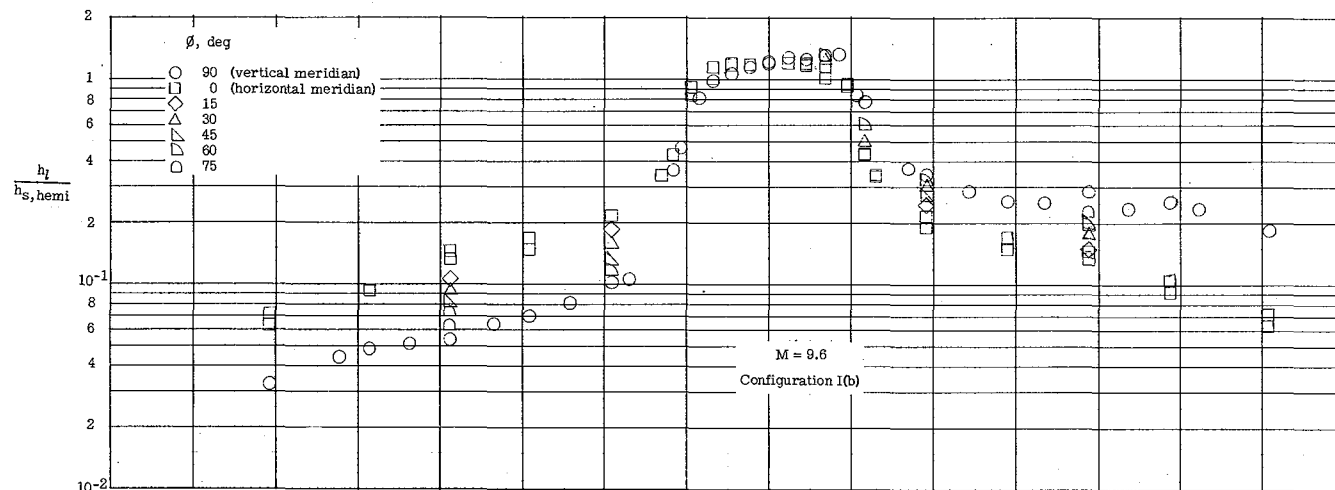
(a) $\alpha = 0^\circ$.

Figure 7.- Heat-transfer distribution over blunt-nose cone at $M = 6.0$ and $M = 9.6$. Configuration I.



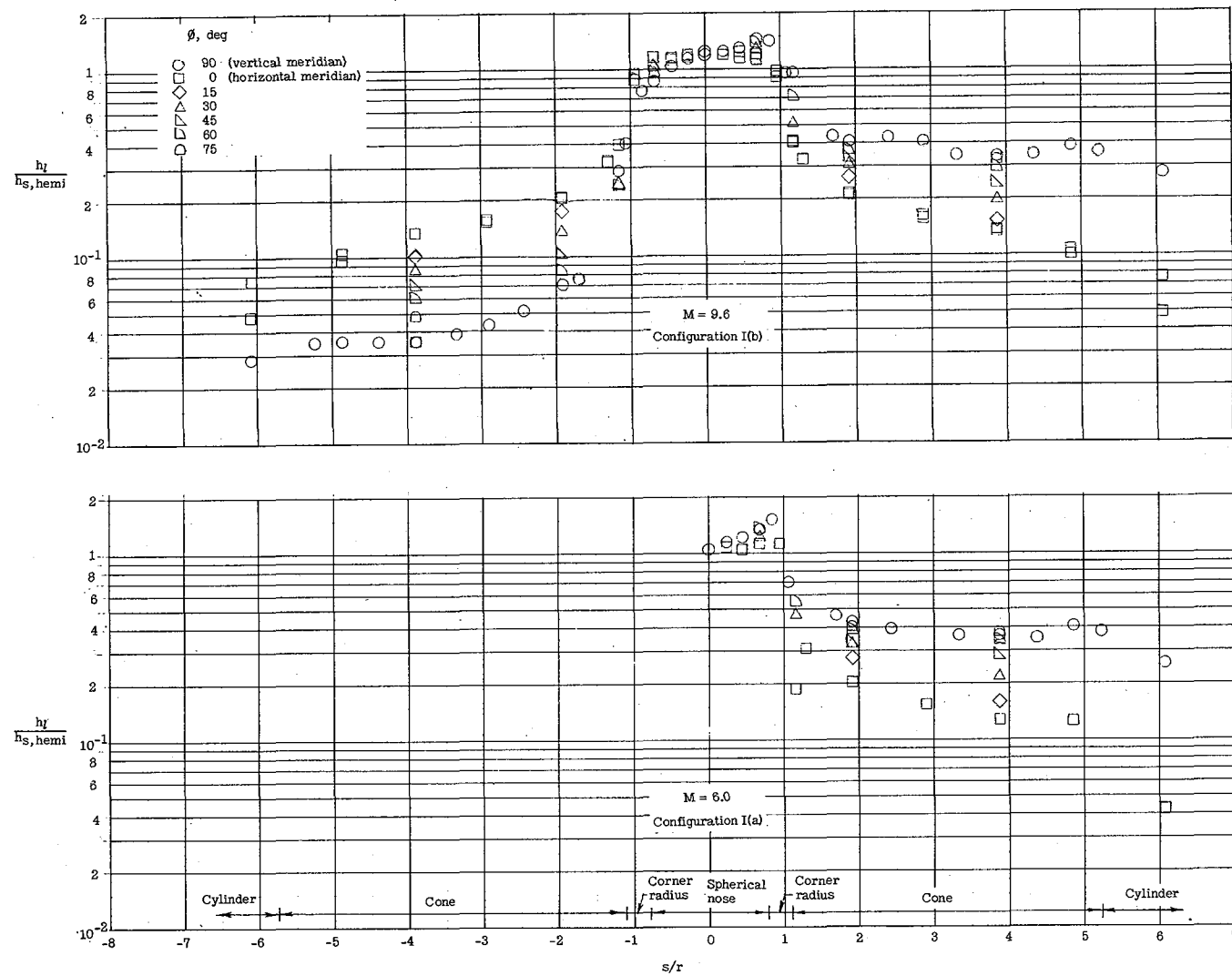
(b) $\alpha = 5^\circ$.

Figure 7.- Continued.



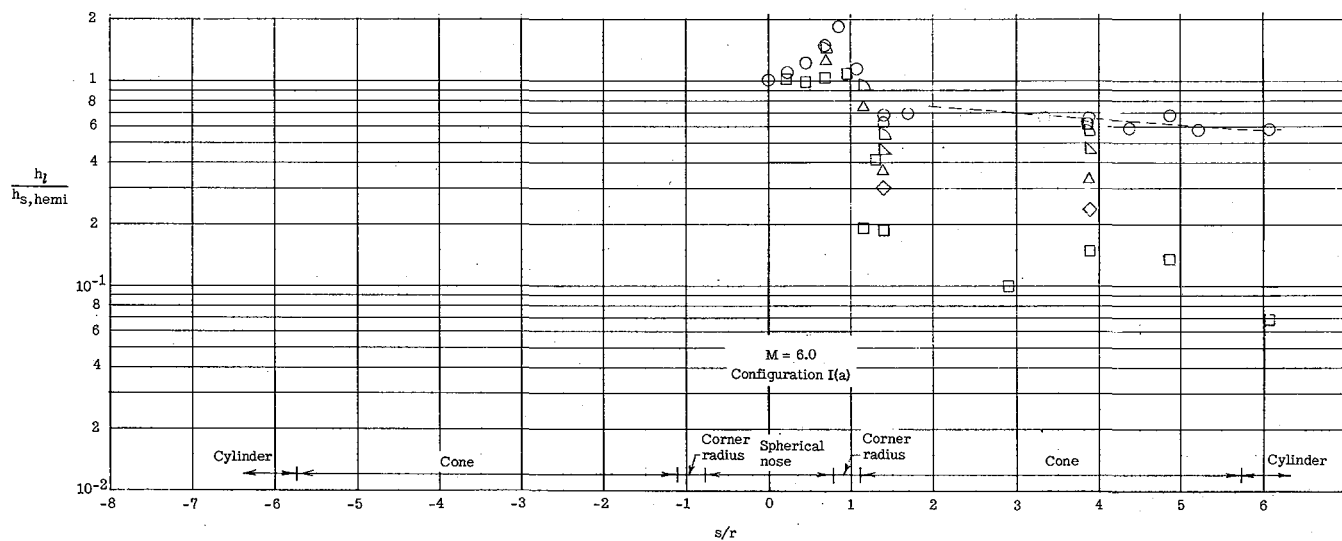
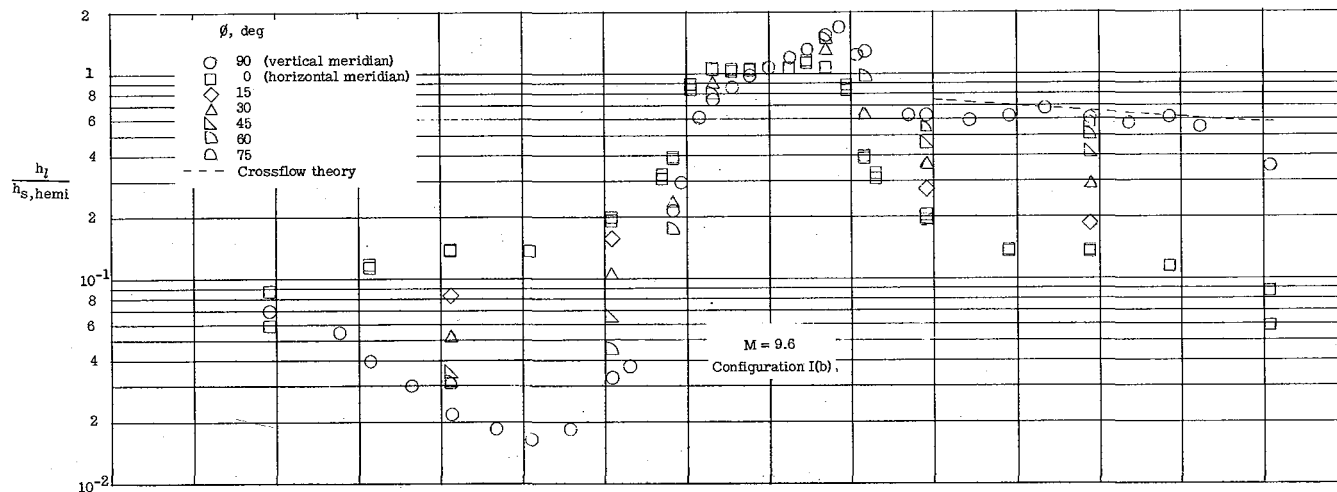
(c) $\alpha = 10^\circ$.

Figure 7.- Continued.



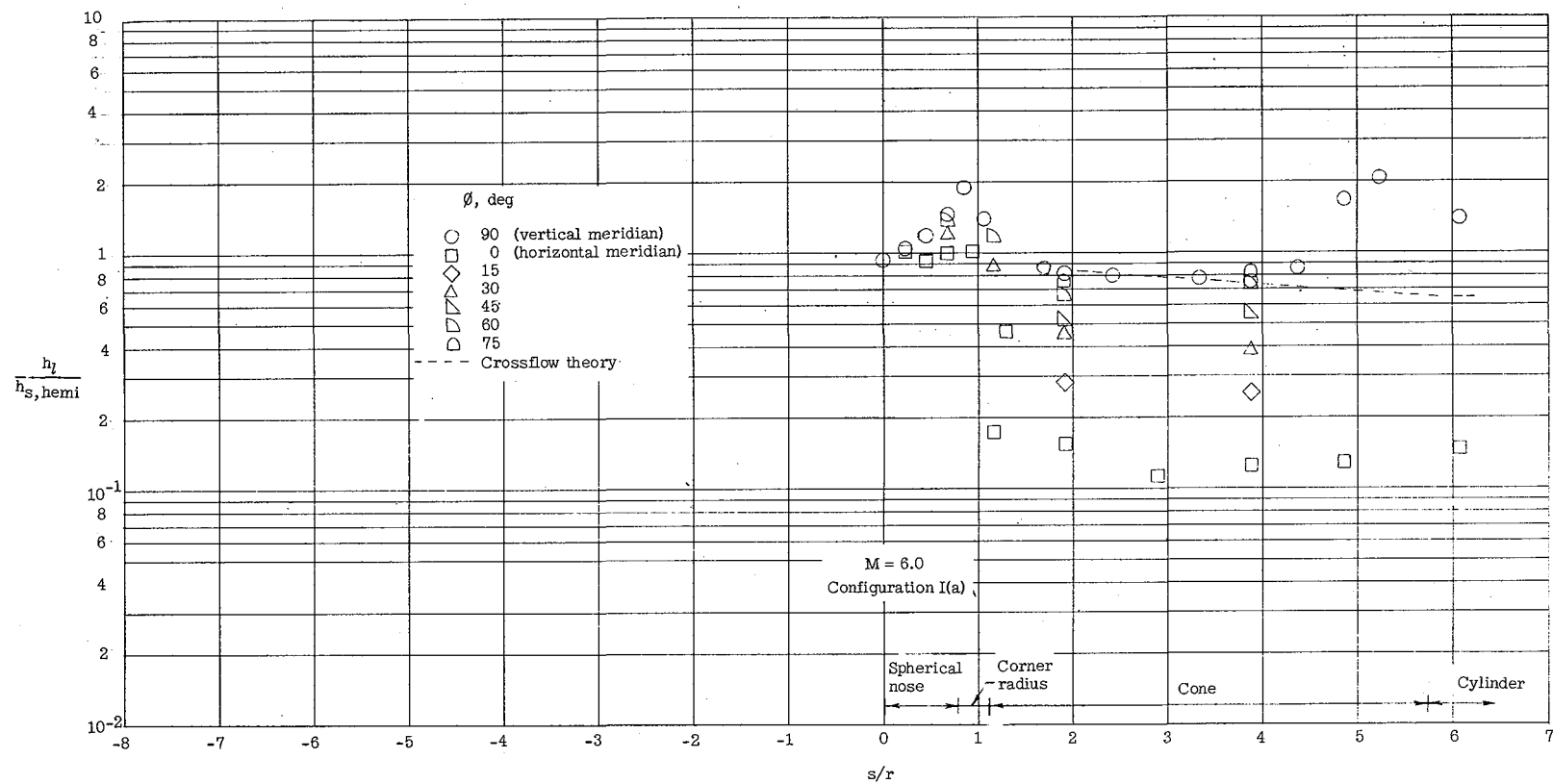
(d) $\alpha = 15^\circ$.

Figure 7.- Continued.



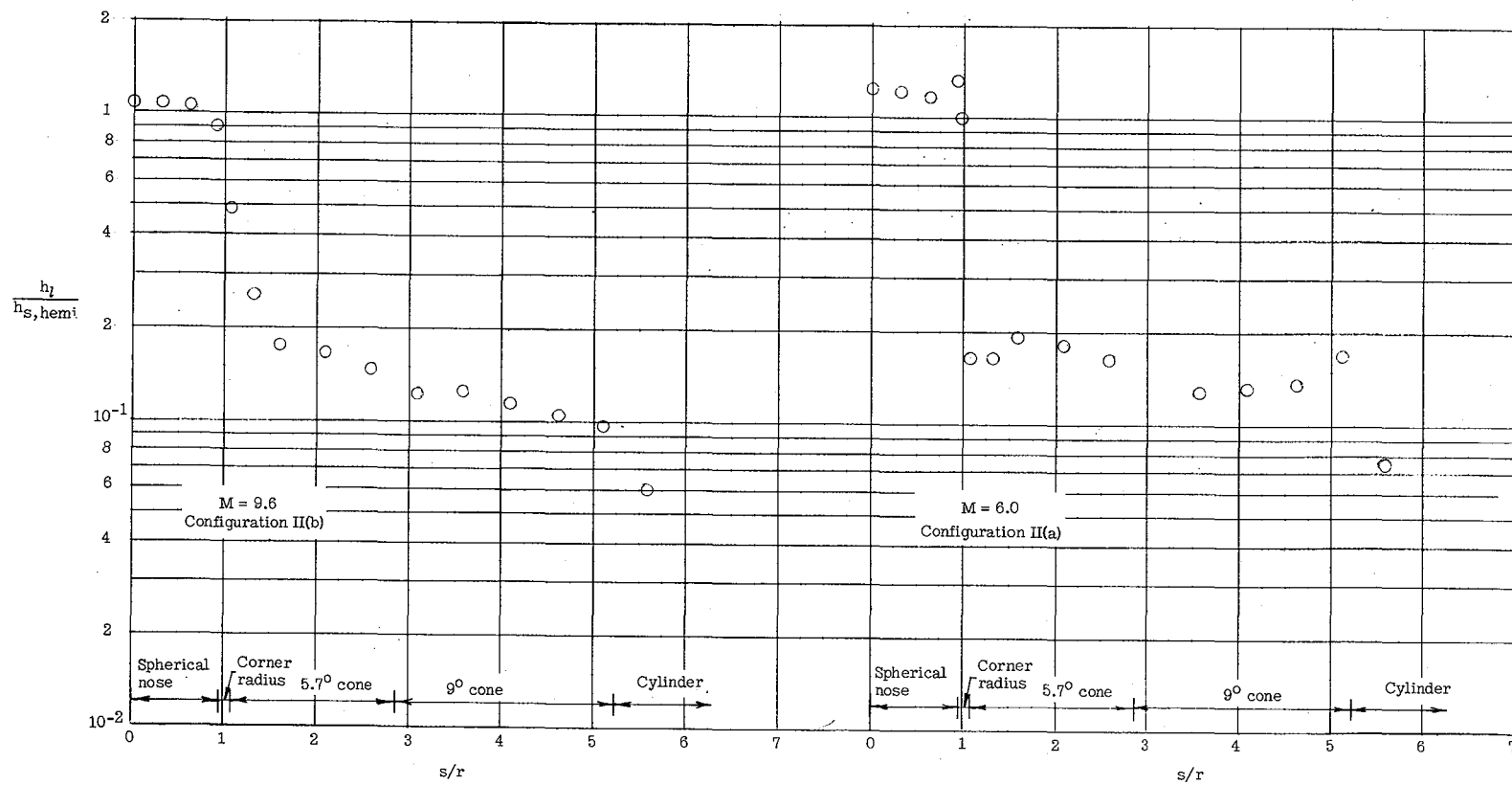
(e) $\alpha = 25^\circ$.

Figure 7.- Continued.



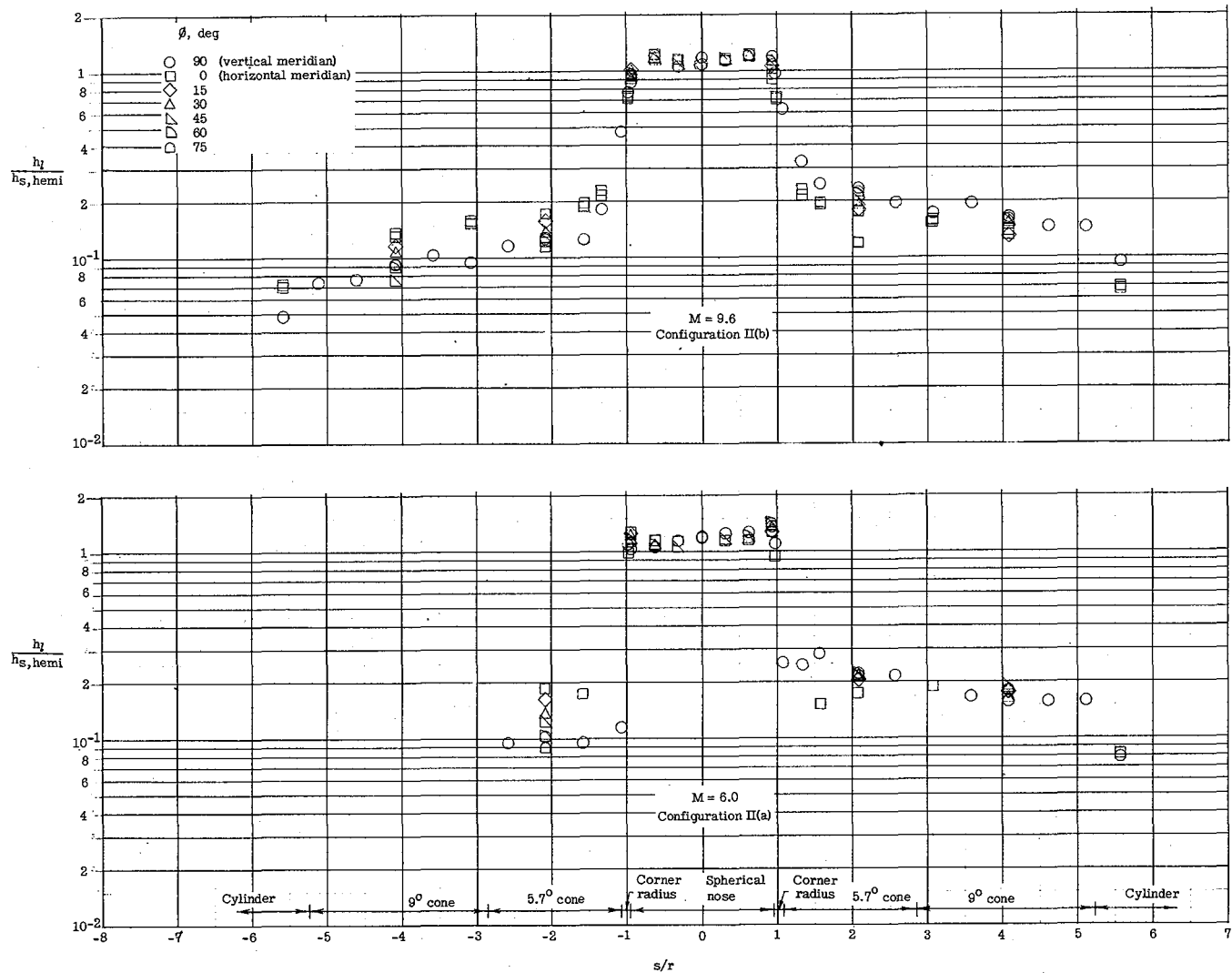
(f) $\alpha = 30^\circ$.

Figure 7.- Concluded.



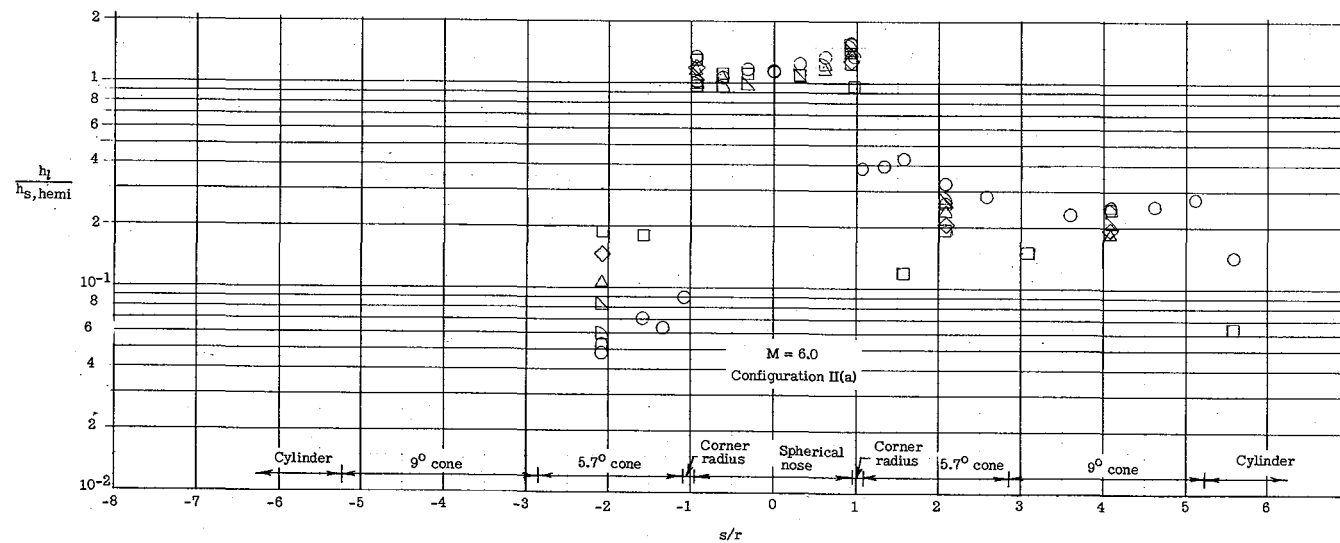
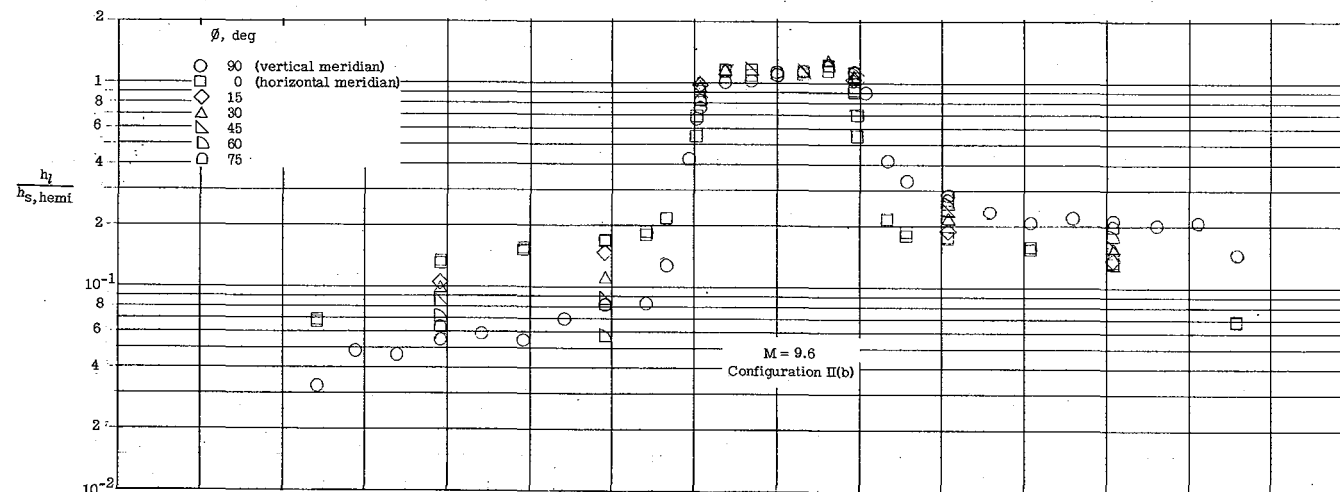
(a) $\alpha = 0^\circ$.

Figure 8.- Heat-transfer distribution over blunt-nose cone at $M = 6.0$ and $M = 9.6$. Configuration II.



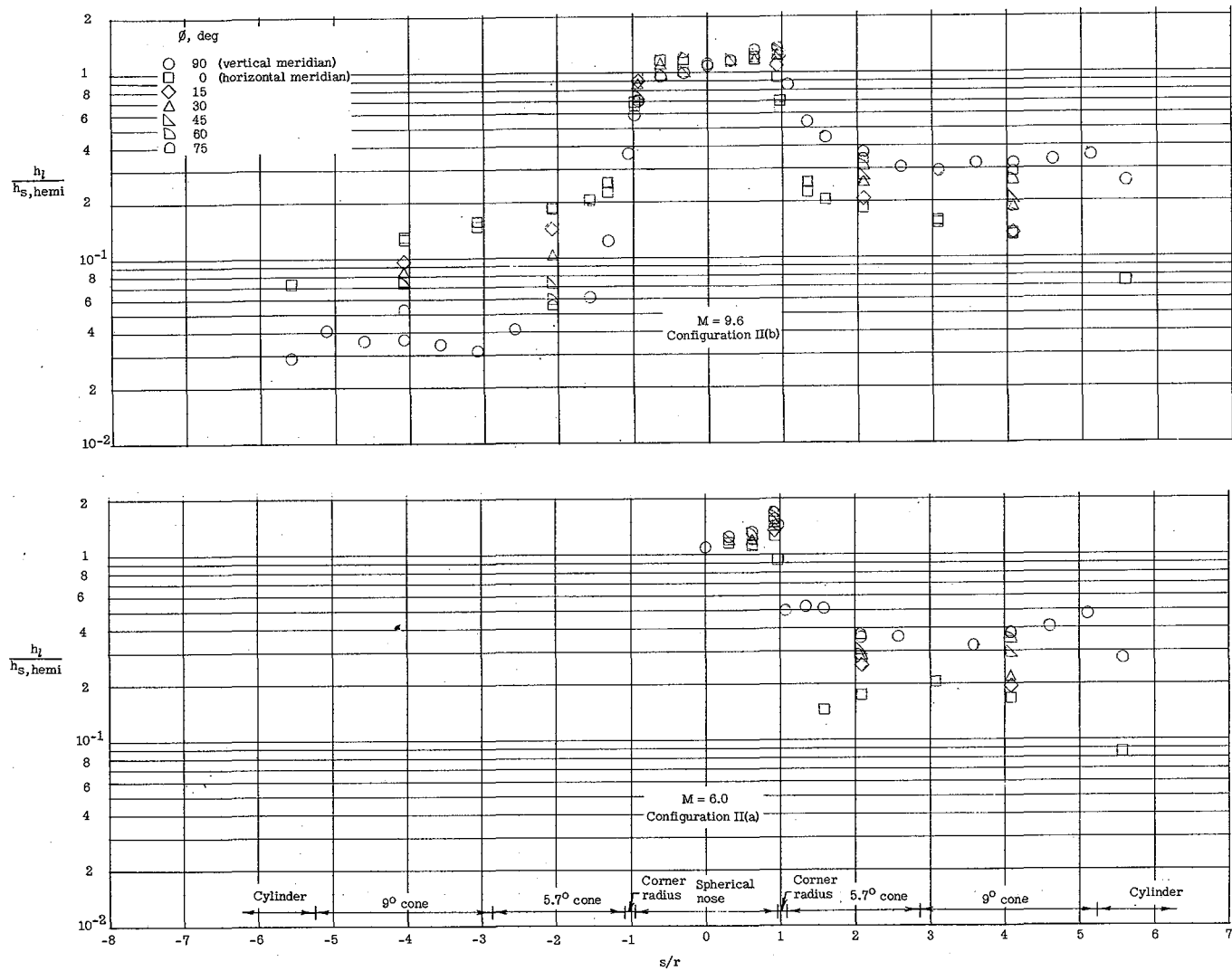
(b) $\alpha = 5^\circ$.

Figure 8.- Continued.



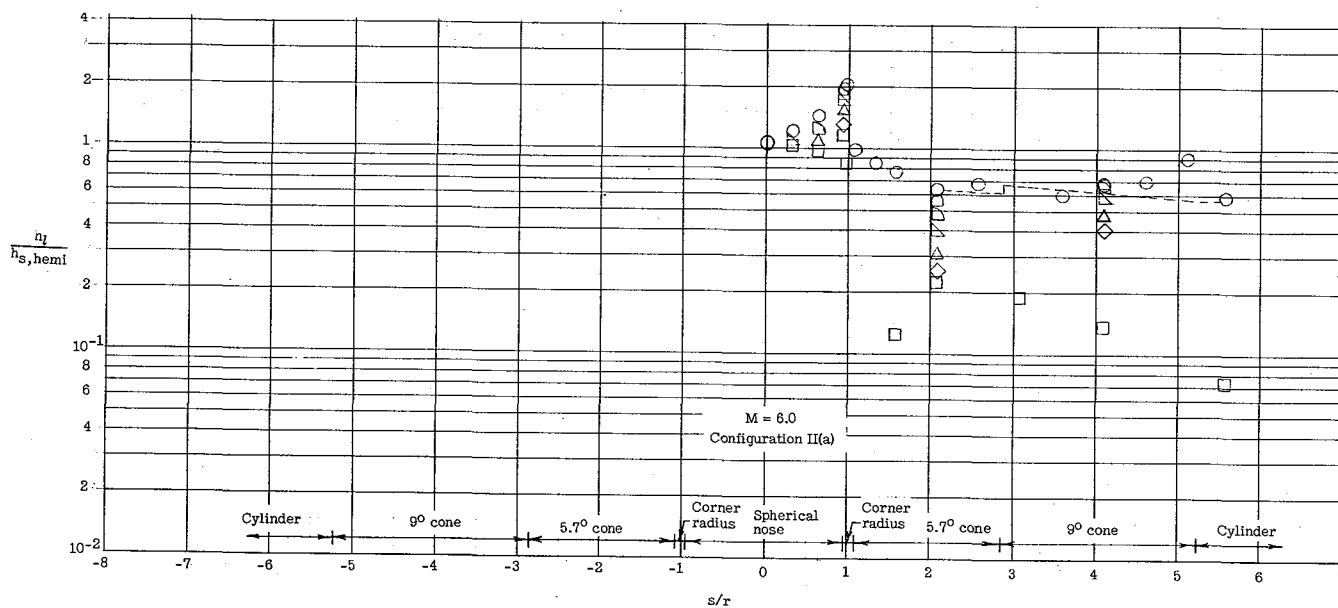
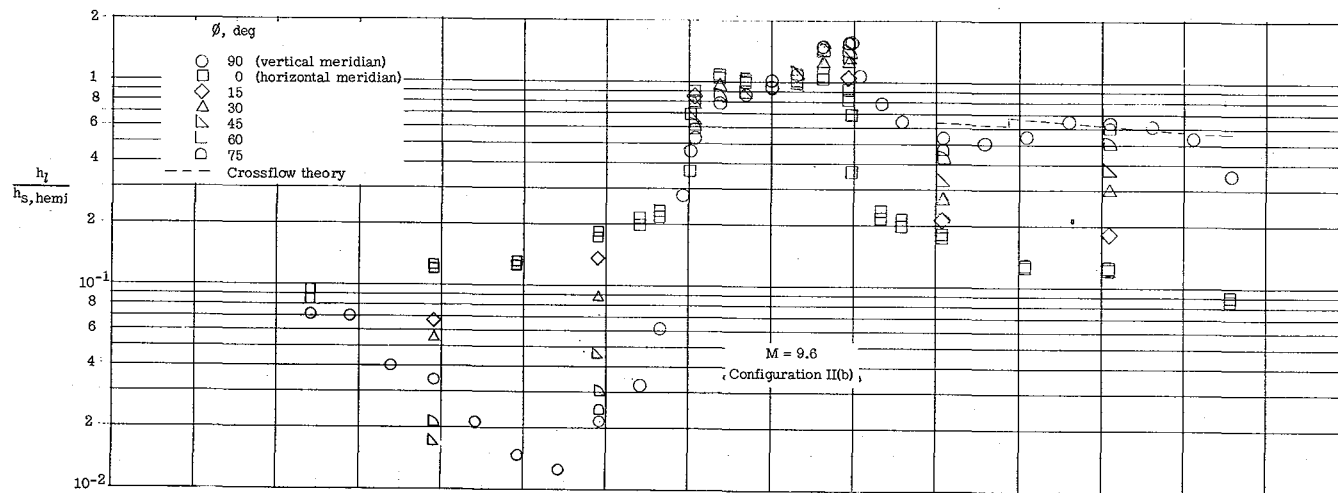
(c) $\alpha = 10^\circ$.

Figure 8.- Continued.



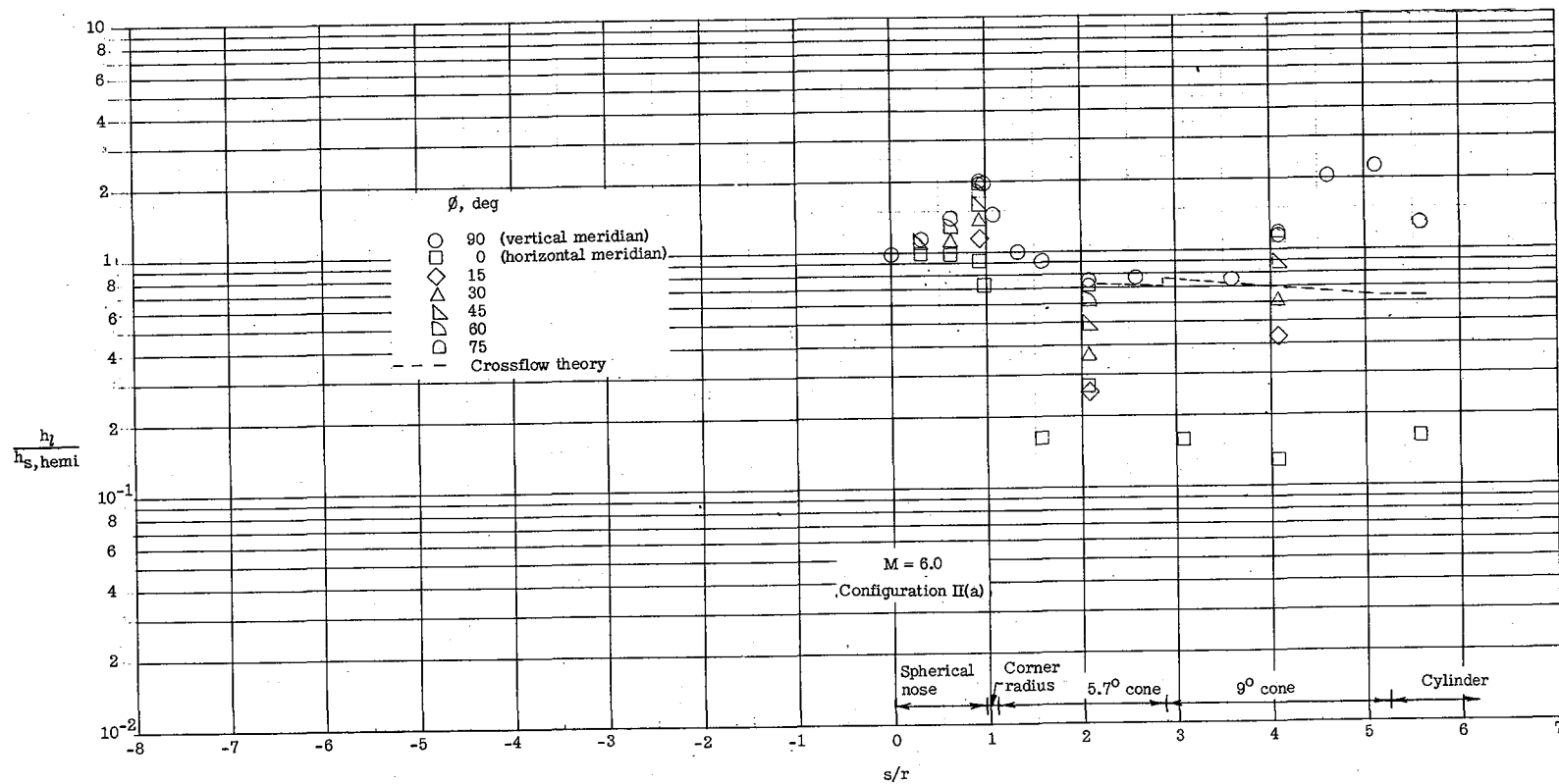
(d) $\alpha = 15^\circ$.

Figure 8.- Continued.



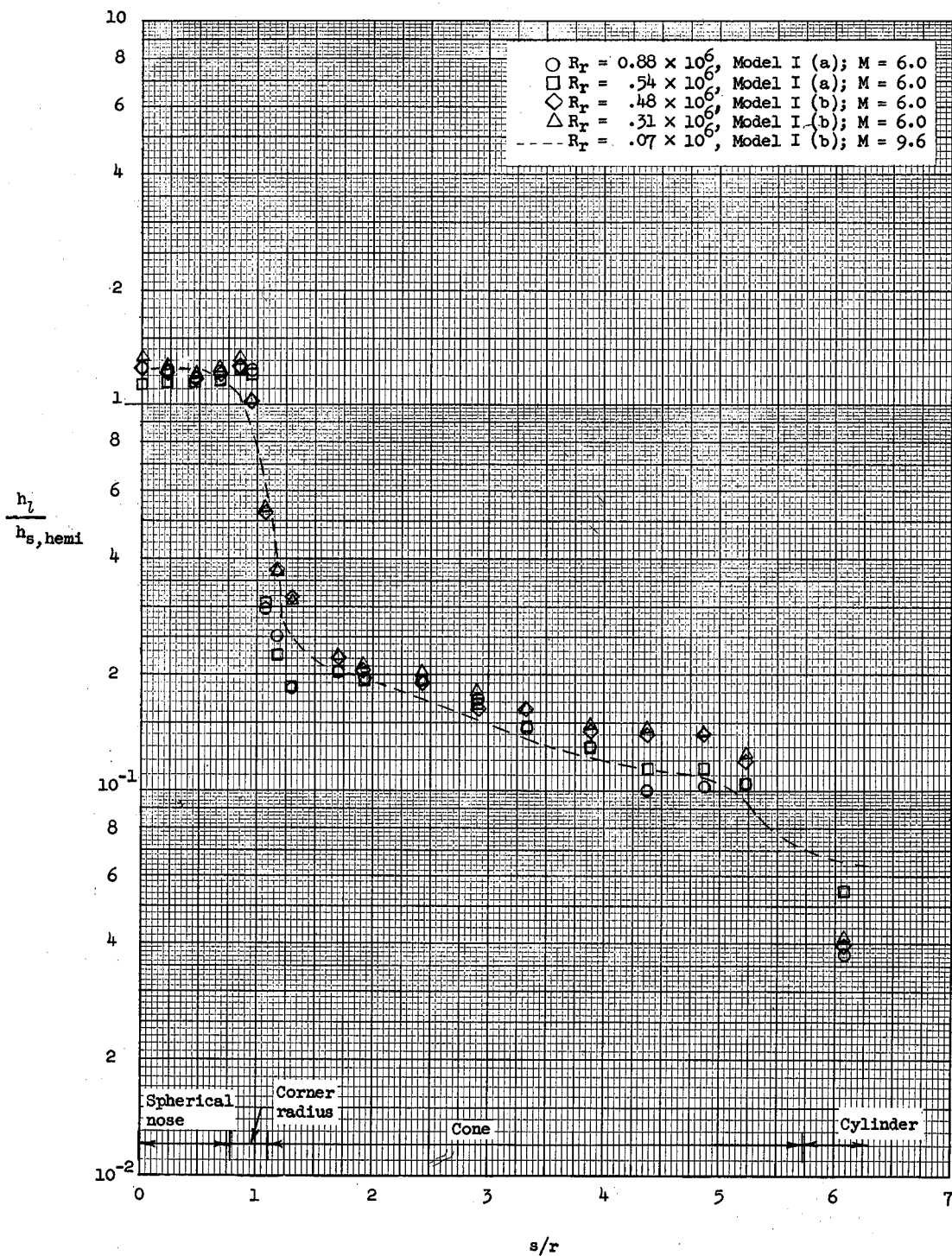
(e) $\alpha = 25^\circ$.

Figure 8.- Continued.



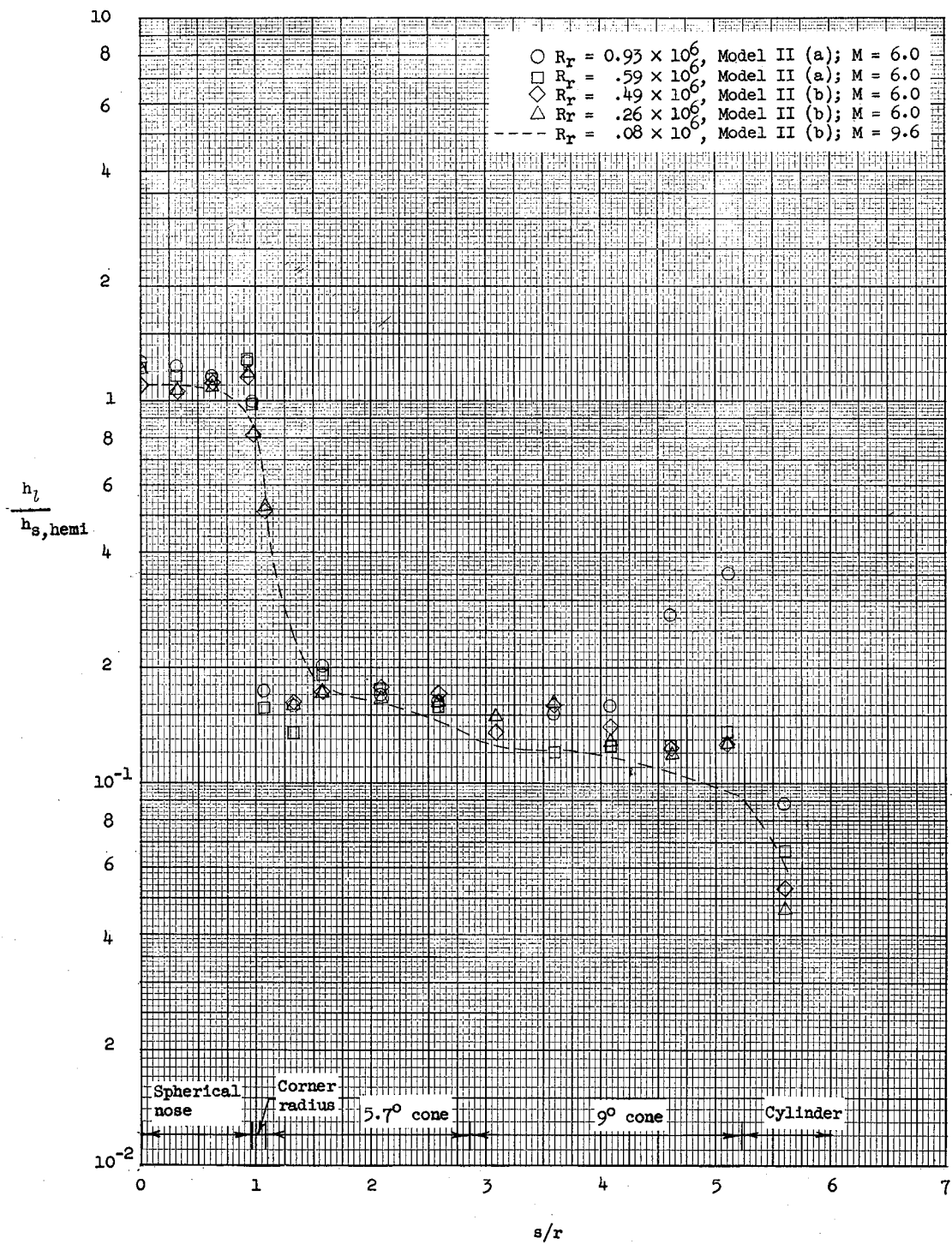
(f) $\alpha = 30^\circ$.

Figure 8.- Concluded.



(a) Configuration I.

Figure 9.- Reynolds number effect on heat-transfer distribution at an angle of attack of 0° .



(b) Configuration II.

Figure 9.- Concluded.

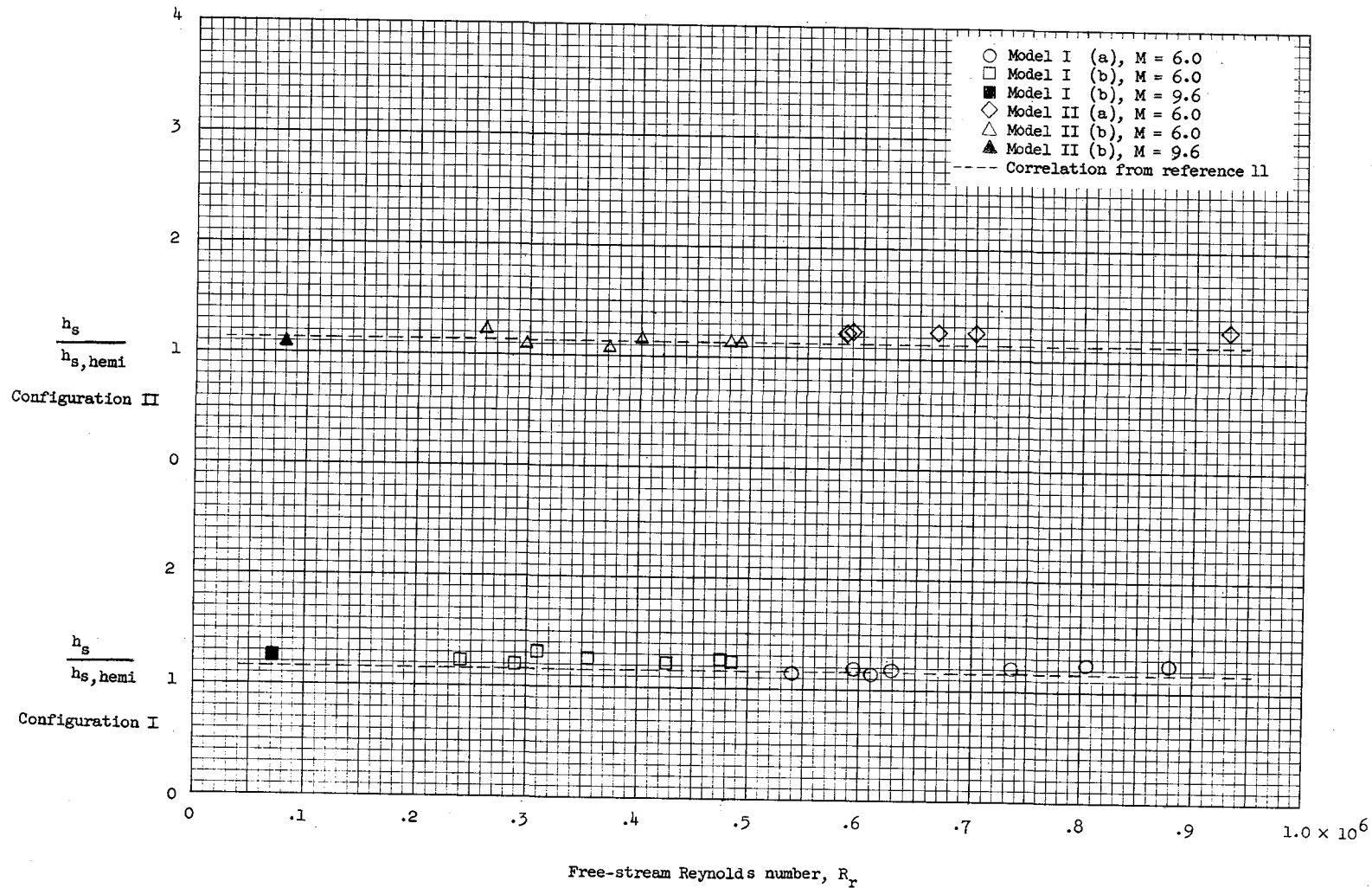
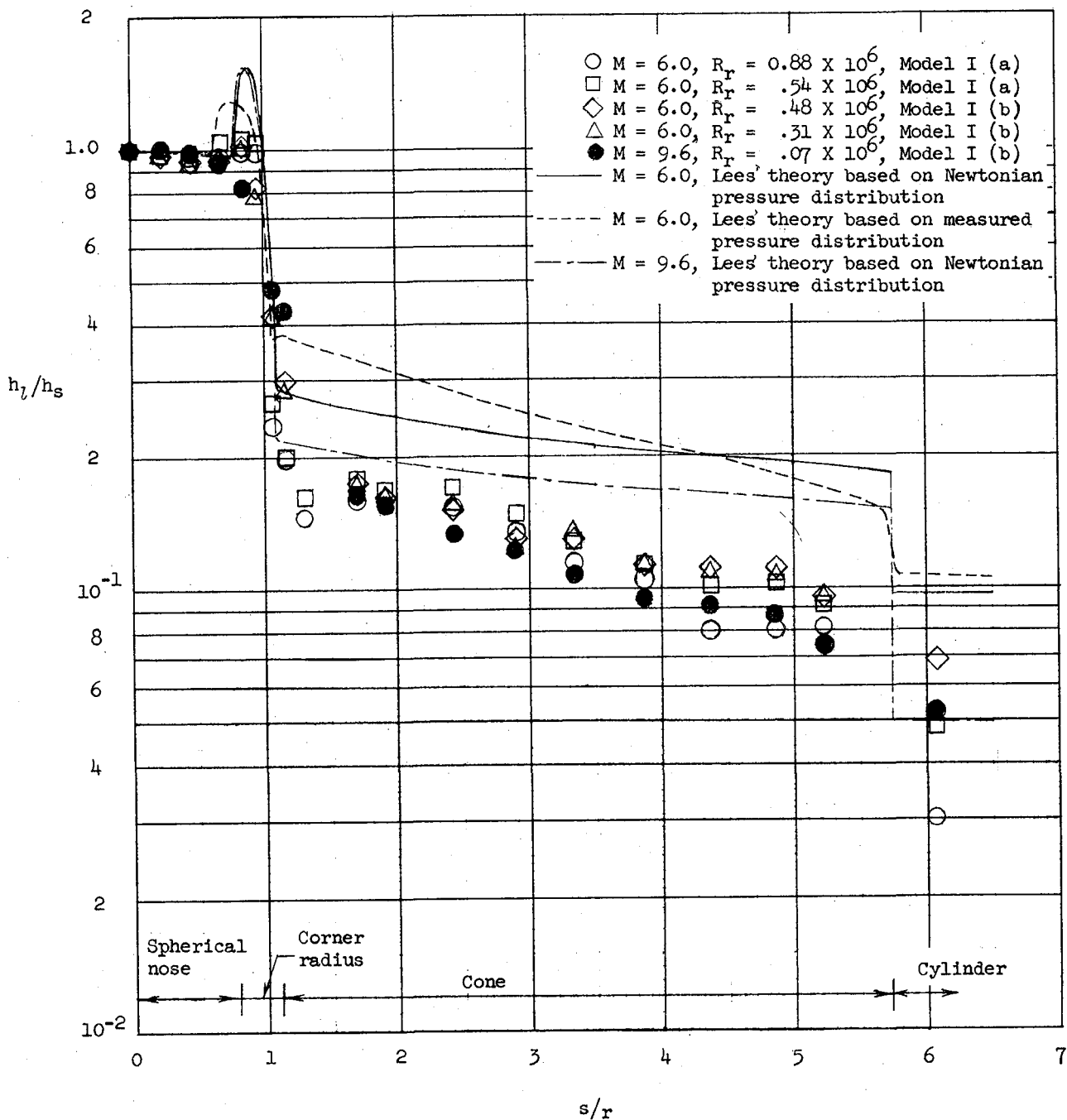
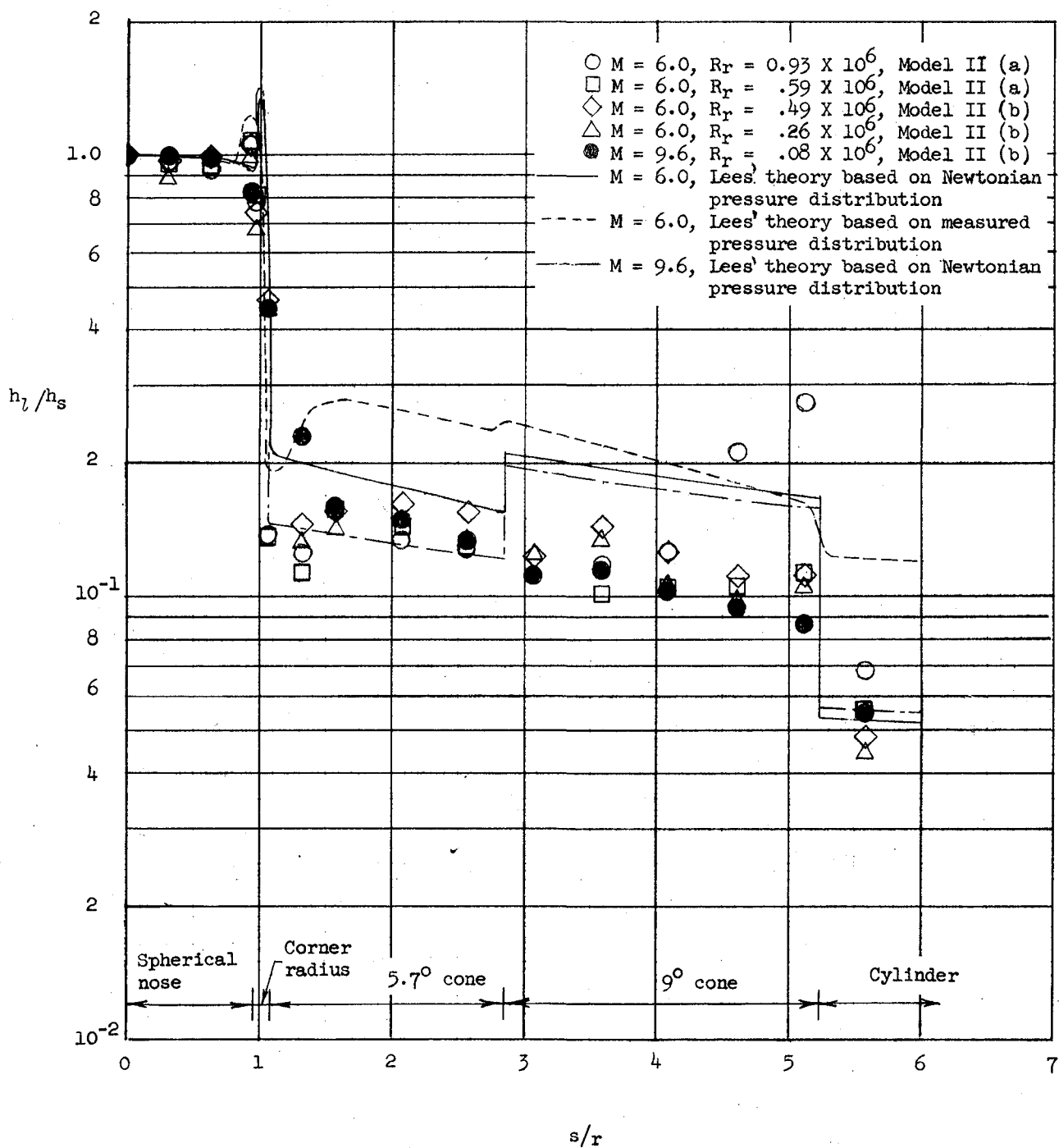


Figure 10.- Reynolds number effect on stagnation heating at an angle of attack of 0° .



(a) Configuration I.

Figure 11.- Comparison of heat-transfer distributions for $\alpha = 0^\circ$ over the full Reynolds number range investigated with distributions predicted by the theory of Lees.



(b) Configuration II.

Figure 11.- Concluded.